(2)

Office of Naval Research
Contract N00014-87-K-0326
Technical Report No. UWA/DME/TR-89/2

Toughening of a Particulate-Reinforced/Ceramic-Matrix Composite

M. Taya, S. Hayashi, A.S. Kobayashi and H.S. Yoon

September 1989

The research reported in this technical report was made possible through support extended to the Department of Mechanical Engineering, University of Washington, by the Office of Naval Research under Contract N00014-87-K-0326. Reproduction in whole or in part is permitted for any purpose of the United States Government.

Abstract

The micromechanics involved in increased crack growth resistance, K_R, of a TiB_2 particulate-reinforced/SiC-matrix composite over that of a monolithic SiC was analyzed experimentally and theoretically. Fractography studies showed that the advancing crack was attracted to the particulates due to the tensile region surrounding the particulate. Countering this effect was the compressive thermal residual stress in the matrix, which resulted in the toughening of the composite. This thermal residual stress field in a particulate reinforced ceramic matrix composite is induced by the mismatch in the coefficients of thermal expansions of the matrix and the particulate when the composite was cooled from the processing to room temperatures. The increase in, K_R, of the TiB_2-particulate/SiC-matrix over the monolithic SiC matrix, measured by using an hybrid experimental-numerical analysis, was 77 percent, and compared well with the analytically predicted increase of 52 percent. The increase in K_R predicted by the crack deflection model was 14 percent. Dependance of K_R on the volume fraction of the particulates and of voids is also discussed

I. Introduction

The primary toughening mechanisms of particulate reinforced ceramics have been attributed to: (i) interaction between the crack front and particulates (crack front bowing model)[1-2]; (ii) crack deflection by the particulates in front of a propagating crack (crack deflection model);[3] and (iii) crack bridging by ductile particulates (particulate bridging model).[4] Other secondary mechanisms which contribute to the toughening of ceramic composites are: (iv) residual stress (strain) field due to mismatch between the coefficients of thermal expansion (CTEs) of the ceramic matrix and particulates;[5,6] and (v) the grain size.[7]

Increase in the fracture toughnesses, K_c, of particulate-reinforced/ceramic-matrix composites with modest particulate volume fractions, $f_p \cong 0.1\sim0.3$, over the fracture toughness of unreinforced ceramic matrix, K_m, vary from 10 percent[7] and 40 to 70 percent[5,6,8,9]. This increase in the fracture toughness was attributed to crack front deflection. Several investigators have observed such crack deflection due to particulates in particulate reinforced ceramic matrix composites.[3,5,8] Such crack deflection was also observed in monolithic ceramics and was considered a major contributor to the toughening of ceramics,[10] although the crack deflection in monolithic ceramics takes place along the grain boundary. The crack deflection observed in particulate-reinforced/ceramic-matrix composites, however, was much larger in magnitude, and was thus considered a dominant toughening mechanism.

The crack deflection model of Faber and Evans[3] is based on a geometrical treatment of a crack deflected from its main crack plane and ignores the local stress field at and near the interface between the matrix and the filler (particulate in this paper). This local stress is caused by the difference in the stiffnesses and/or the coefficient of thermal

expansion (CTE) between the matrix and particulate. The crack deflection model predicts the toughness ratios of K_c/K_m = 1.12~1.15 for uniformly distributed particles and for particle volume fractions of f_p = 0.1~0.3. This K_c/K_m ratio predicted by the crack deflection model is smaller than 1.4–1.7, typically observed in most particulate reinforced ceramic matrix composites.[5,6,8,9] Thus, the crack deflection model only accounts for a portion of the increase in the toughness. An additional toughening mechanism which has been identified in fiber-reinforced/ceramic-matrix composite is fiber bridging in the region behind a crack tip.[11–15] The fiber bridging model, however, is only applicable to short and continuous fiber composites and not to a particulate reinforced composite. A similar idea has recently been used by Budiansky et al. (1988) to account for the toughening of a ceramic by the bridging of ductile metal particulates, which deform elastically/plastically until failure. This model is valid for ductile metal particulates, but is not valid for brittle particulates such as an intermetallic compound, for example, TiB_2. Moreover, it is much less likely that TiB_2 particulates located on the crack plane will break.

An additional mechanism, which can contribute to the toughening of a particulate-reinforced/ceramic-matrix composite, is the thermal residual stress field caused by the mismatch of CTEs between the matrix and the particulates. The role of thermal residual stress induced by CTE mismatch has been considered as a major cause for the crack deflection by Wei and Becker,[5] although no quantitative estimate on the increased toughness was made. In principle, quantitative analysis of toughening due to crack deflection by thermal residual stress can be made within the framework of the Fable-Evan's crack deflection model, but such an analysis would become intractable. Another toughening mechanism that has *not* been studied so far is the thermal residual stress in the *matrix domain*. If such residual stress in the matrix is to contribute to toughening, then the thermal residual stress in the matrix must be compressive. This negative thermal residual stress in the matrix can exist when the CTE of the particulate exceeds that of the matrix. This is indeed the case with the TiB_2-particulate/SiC-matrix[6,8,9] and TiC-particulate/SiC-matrix composites.[5]

In order to quantify the influence of thermal residual stress, a combined experimental and theoretical analysis on the TiB_2/SiC composite as a model system was undertaken. Experimental analysis, followed by a brief description of the analytical model will be presented in Sections II and III, respectively. Finally, a comparison between the experimental and theoretical results will be presented in Section IV.

II. Experiment

2.1 Materials

The ceramic matrix composite considered is a 16 percent volume TiB_2 particulate/SiC matrix (TiB_2/SiC) composite. The unreinforced SiC and TiB_2/SiC

composite* were processed by pressureless sintering in an inert atmosphere at a temperature in excess of 2000°C. The room temperature material properties of SiC matrix and TiB_2 particulate are given in Table 1.[6,16,17]

The temperature dependency of the CTE of SiC and TiB_2 within the temperature range of 200 to 2200K[16,17] is given in Fig. 1, and is used in Section III to calculate the thermal residual stresses induced by the CTE mismatch between the matrix and the particulate.

Photographs of typical backscattered electron image (BEI) of as-processed monolithic SiC and TiB_2/SiC composite are shown in Fig. 2(a) and (b), respectively. In Fig. 2(b), the isolated light gray areas and the continuous domain of gray are TiB_2 particulates and SiC matrix, respectively, where the dark isolated spots indicate voids. Voids are also seen in the unreinforced SiC as dark spots in Fig. 2(a). Some of the voids in Fig. 2(b) appear to be TiB_2 particulates, which fell out during polishing, due to weak bonding of the matrix-particulate.[6] A number of BEI photos similar to that of Fig. 2(b) were used to measure the average interparticulate spacing, λ (between the centers of two particulates), and the volume fraction of voids, f_v (based on ASTM Standard E562–76[18]). The results are $\lambda = 11.1\mu m$ and $f_v = 0.016$, which will be used in the analytical model. The value of f_v so measured is consistent with the density of the composite, i.e., $(1-f_v) \equiv 0.98–0.99$ reported by McMurty et al.[6]

2.2 Measurement of Crack Growth Resistance, K_R

The method of obtaining crack growth resistance, K_R, is based on a hybrid experimental-numerical analysis[20] where moire interferometry was used. The purpose of using moire interferometry was to measure the crack opening displacement (COD) along the crack as well as at the load point. A schematic of the moire interferometry system used in this study is shown in Fig. 3. A moire specimen with an argon laser of 514.5 nm wavelength, a grating, F, of 600 lines/mm and a virtual grating of 2F = 1200 lines/mm were used. The displacement, u, can be measured by counting the number of the moire fringe N[19]

$$u = \frac{N}{2F} \tag{1}$$

The specimen used is a chevron-notched, a wedge-loaded double-cantilever beam (WL-DCB) type, which is shown in Fig. 4 where the dimensions unit are in mm. A side groove with a depth of one half of the specimen thickness was used to propagate a straight crack along the crack plane (x-axis). A chevron notch was used to generate a true crack. The effect of the side groove on the stress intensity factor is minimal.[21] The moire interferometry grating, which consists of a thin aluminum film on an epoxy adhesive, is attached to the front side (not the groove side). The displacement along the

* Supplied by British Petroleum Company, Niagara Falls, N.Y.

y-axis, u_y, on the front side is measured by the moire during loading. As shown in Fig. 4, the length of a two-dimensional crack, a, is measured from the intersection of the chevron notch with the front side (x = 0, y = 0). A typical moire fringe pattern of a TiB_2/SiC composite specimen is shown in Fig. 5. The displacement, u_y, along the x-axis, i.e., the one-half crack opening displacement (COD) was measured by taking the average of the u_y values on the left and right side fringes since the fringe pattern is often unsymmetrical as shown in Fig. 5

For the hybrid analysis, the u_y at the load point, i.e., the contact point with the WL-DCB specimen, together with the measured vertical load, p_x, are input to a two-dimensional finite element code for computing the stress intensity factor, K_I. This procedure eliminates the uncertainty in numerical analysis associated with the friction at the loading pin-specimen contact. The boundary conditions and the pattern of the finite element analysis are shown in Fig. 6 where only one half of the WL-DCB specimen was used for the analysis. The results of the COD measured (symbols) and predicted by the finite element analysis (solid curves) are plotted as a function of x for various stages of loading in Fig. 7. This finite element analysis was validated by the excellent agreement between the computed and measured (by moire interferometry) CODs along the crack plane in Fig. 7. Finite element analysis was then used to compute the stress intensity factor using the standard strain energy release rate method. This procedure was repeated for each incremental increase in crack length, Δa, which then yielded the crack growth resistance K_R.

Crack growth resistance curves, K_R–Δa, were thus obtained for the monolithic SiC and TiB_2/SiC composites under monotonically increasing load as shown in Fig. 8(a), and cyclically increasing load as shown in Fig. 8(b). The resultant K_R–Δa relations are shown in Fig. 9 where the circles and the squares denote the monolithic SiC and TiB_2/SiC composites, respectively. The open and filled symbols represent the results of monotonic and cyclic loadings, respectively. Fig. 9 shows that K_R of the composite increased by 60 percent (cyclic loading) ~ 80 percent (monotonic loading) over that of the monolithic SiC. Such increases in K_R cannot be predicted by the existing models alone, since the toughness increase predicted by the crack deflection model[3] is only 14 percent above the monolithic matrix and is much lower than that obtained experimentally.

III. Analytical Model

The analytical modeling consists of two steps. The first step is to calculate the average thermal residual stresses in the matrix and reinforcement by using the Eshelby's model[22] which is modified for a finite volume fraction of particulates.[23–26] The second step is to calculate the change in the mode I stress intensity factor, ΔK, due to the compressive residual stress (obtained in the first step) in the matrix. In this model, the crack is assumed to propagate toward the nearest tensile stress region, which coincides with the domain surrounding the particulate generated by the thermal residual stress.

3.1 Thermal Residual Stress

A particulate composite is assumed to consist of three phases: spherical particulates of volume fraction f_p, spherical voids of volume fraction f_v and the matrix with its volume fraction of $1-f_p-f_v$. In order to calculate the thermal residual stress in a composite at room temperature, T_R, the composite is assumed to be subjected to a temperature change, $\Delta T = T_R - T_P$ where T_P denotes the processing temperature such as sintering temperature. The thermal residual stresses in a composite are assumed to be induced by elastic deformations of the matrix and particulates under a uniform ΔT. The voids are included since the SEM observation of Fig. 2 shows numerous voids distributed in a composite, despite the small volume fraction ~1.6 percent.

The modified Eshelby's model is suited for calculating the average internal stress field in a composite.[26,27] The particulate composite containing voids subjected to uniform temperature change, ΔT, is schematically shown in Fig. 10(a) where the domains of the particulates, voids, and the entire composite are denoted by Ω_1, Ω_2 and D respectively, thus the matrix domain becomes $D-\Omega_1-\Omega_2$. The elasticity problem of Fig. 10(a) can be reduced to that of Fig. 10(b) where the CTE's and ΔT are converted to the CTE misfit strains, $\underset{\sim}{\alpha}^1$ (in Ω_1) and $\underset{\sim}{\alpha}^2$ (in Ω_2), which are given by

$$\underset{\sim}{\alpha}^1 = \int_{T_P}^{T_R} (\alpha_p - \alpha_m)\underset{\sim}{\delta}\, dT \tag{2}$$

$$\underset{\sim}{\alpha}^2 = \int_{T_P}^{T_R} (\alpha_v - \alpha_m)\underset{\sim}{\delta}\, dT \tag{3}$$

and where α_p, α_v and α_m are the CTEs of the particulate, void and matrix, respectively, and $\underset{\sim}{\delta}$ is the isotropic tensor (Kronecker's delta). The subscripted tilda denotes a tensorial quantity. α_v is not involved in the final formulation since the stiffness of Ω_2 vanishes.

The modified Eshelby's model Fig. 10(b), is equivalent to Fig. 10(c) where two inhomogeneities (Ω_1,Ω_2), with the misfit strains defined by eqs. (2) and (3) are replaced by the inclusions with eigenstrains of $\mathbf{e}^1$ in Ω_1 and $\mathbf{e}^2$ in Ω_2. The thermal stresses in a composite can then be solved in terms of the eigenstrains. Detailed formulation for the thermal stresses in a particulate composite containing voids is given in the Appendix. Only the average thermal stresses, which will be used later in this section for calculations of the stress intensity factor change, ΔK, will be considered. The average stress field in the particulate $\langle\sigma\rangle_p$ and in the matrix $\langle\sigma\rangle_m$ are isotropic since the particulate reinforcement and the CTE misfit strains are dilatational. From the Appendix, these are

$$\frac{\langle\sigma\rangle_p}{E_m} = \frac{-2(1-f_p-f_v)\beta\alpha_1^*}{A} \tag{4}$$

$$\frac{\langle\sigma\rangle_m}{E_m} = \frac{2f_p\beta\alpha_1^*}{A} \tag{5}$$

where

$$A = (1-f_v)\left[\left\{1-\frac{f_p}{(1-f_v)}\right\}(\beta+2)(1+\nu_m) + \frac{3\beta f_p(1-\nu_m)}{(1-f_v)}\right]$$

$$\beta = \left(\frac{1+\nu_m}{1-2\nu_p}\right)\left(\frac{E_p}{E_m}\right) \tag{6}$$

f_p and f_v are the volume fraction of the particulates and voids, respectively. E_i and ν_i are the Young's modulus and Poisson's ratio of the i-th phase, where i = m and p represent the matrix and particulate, respectively. When the composite does not contain voids, the above equations can be simplified as

$$\frac{\langle\sigma\rangle_p}{E_m} = \frac{-2(1-f_p)\beta\alpha_1^*}{A} \tag{7}$$

$$\frac{\langle\sigma\rangle_m}{E_m} = \frac{2f_p\beta\alpha_1^*}{A} \tag{8}$$

where

$$A = (1-f_p)(\beta+2)(1+\nu_m) + 3\beta f_p(1-\nu_m) \tag{9}$$

It is clear from the above equations that the thermal residual stresses are influenced by a number of factors: the particulate-matrix stiffness ratio; the Poisson's ratios of the matrix and particulate; the volume fractions of the particles and voids; and the CTE misfit strain, $(\alpha_p-\alpha_m)\Delta T$. The formula used by Wei and Becker does not contain the volume fraction of the particulates, f_p, thus it is a lower order approximation to the stresses in a composite with a finite volume fraction of particulates.

For a particulate reinforced ceramic matrix composite with $\alpha_p > \alpha_m$, such as a TiB_2/SiC composite, $\alpha_1^* < 0$ as seen from eqs. (5) and (6) the average thermal stresses in the particulates and matrix are in tension and compression, respectively. The thermal residual stress field in a TiB_2/SiC composite consists of two regions: the tensile stress region in the particulates and their vicinity in the matrix, and the compressive stress region in the bulk of the matrix, as shown schematically in Fig. 11.

3.2 Stress Intensity Factor Reduction Due to Thermal Residual Stress in Matrix

Consider a semi-infinite crack surrounded by a particulate-reinforced/ceramic-matrix composite with a thermal residual stress distribution as shown in Fig. 11. The semi-infinite crack is assumed to advance from one concentrated tensile region to its

nearest counterpart which may be off the crack plane. Thus, the crack may be deflected according to Wei and Becher,[5] but the general crack path over a number of tensile regions will be that of a self-similar crack extension. Hence, a self-similar crack extension over an average interparticulate spacing, λ will be considered. When a semi-infinite crack advances by a distance λ, which is the interparticulate distance, the crack tip ligament is subjected to the local average compressive stress, q, over the length of λ-d, as shown in Fig. 12, in addition to the superposed tensile field for self-similar crack propagation. "d" denotes the average diameter of TiB_2 particles. The existence of this local stress, q, decreases the stress intensity factor, ΔK_I. According to Tada,[28] this decrease is

$$\Delta K_I = \frac{2}{\pi} q \sqrt{2\pi(\lambda - d)} \tag{10}$$

IV. Results and Discussion

4.1 Results

Using the analytical model developed in the preceding section, the increase in the fracture resistance of a TiB_2 particulate-reinforced/SiC-matrix composite will be predicted. The analysis involves two steps: calculation of the average thermal residual stresses; and ΔK_I.

The formulae for calculating the average thermal stresses in the particle, $\langle\sigma\rangle_p$, and the matrix, $\langle\sigma\rangle_m$, are given by eqs. (4) and (5), or eqs. (7) and (8) for small values of f_v, respectively. The parameters A, β and α_1^* must be calculated first using known input f_p, f_v, ν_m, ν_p, E_p and E_m. Since the measured volume fraction of voids is very small, i.e., f_v = 0.016, eqs. (7) and (8) will be used in this analysis.

The value of the CTE mismatch strain, α_1^*, is defined by eq. (2). The CTE's of the matrix (SiC), α_m, and the TiB_2 particulate, α_p, are given as a function of temperature T(K) in Fig. 1. By taking T_R = 300K and T_P = 2273K and integrating $\alpha_p - \alpha_m$ with respect to T over the entire temperature range from T_P to T_R, eq. (2) yields

$$\alpha_1^* = -5.15 \times 10^{-3} \tag{11}$$

Parameters β and A are calculated using the data in Table 1 and are

$$\beta = 3.50$$
$$A = 6.86 \tag{12}$$

where $f_v = 0$ was assumed. From eqs. (7), (8), (11) and (12) and using $f_p = 0.16$, the average thermal residual stresses are computed as

$$\langle\sigma\rangle_m = -345 \text{ MPa}$$
$$\langle\sigma\rangle_p = 1810 \text{ MPa} \tag{13}$$

Next an estimate of the toughness increase due to the thermal residual stress in the matrix is made. In eq. (10), we set

$$q = \langle\sigma\rangle_m = -345 \text{ MPa}$$
$$\lambda = 11.1 \ \mu m \tag{14}$$
$$d = 3.06 \ \mu m$$

where λ is the average interparticulate spacing which was obtained from ten SEM photos containing 70 TiB_2 particulates. Substituting eq. (14) into (10) yields

$$\Delta K_I = -1.56 \text{ MPa} \tag{15}$$

The compressive residual stress in the matrix thus reduces the stress intensity factor by 1.56 MPa. This reduction in ΔK_I is equivalent to the increase in the crack growth resistance ΔK_R by the same amount. Hence

$$\Delta K_R = 1.56 \text{ MPa} \tag{16}$$

4.2 Discussion

The measured and predicted increases in fracture resistance is now compared. The measured increase in K_R, ΔK_R, can be obtained from Fig. 9 for the case of monotonic loading,

$$\begin{aligned} \Delta K_R &= (K_R)\text{ composite} - (K_R)\text{ monolith} \\ &= (5.3 - 3.0) \text{ MPa} \sqrt{m} \\ &= 2.3 \text{ MPa} \sqrt{m} \end{aligned} \tag{17}$$

It is clear from eqs. (16) and (17) that the major portion of ΔK_R is attributed to toughening due to the thermal residual stress. If we take the toughness ratio between the composite, K_c, and the monolithic matrix, K_m, the measured and predicted values are

$$\frac{K_c}{K_m} = \begin{cases} 1.77 & \text{measured} \\ 1.52 & \text{predicted} \end{cases} \tag{18}$$

The measured ratio is comparable to those reported by others.[6,8] The crack deflection model of Faber and Evans[3] predicts a K_c/K_m ratio of 1.14 for uniformly distributed TiB_2 particulates. Thus, the crack deflection model cannot account fully for the toughening of a ceramic matrix composite.

The predicted value of K_c/K_m = 1.52 is based on the assumption that T_P = 2273 K which is close to the sintering temperature of the composite and also that both constituent phases of SiC and TiB_2 deform elastically during the cool down process from 2273K to 300K. SiC α-phase matrix is less susceptible to creep than other ceramics at a given high temperature due to its strong covalent bond and ionicity. Its activation energy for self diffusion is large and results in a slow diffusion rate and thus slow creep-rate.[29] This slow creep-rate gives rise to small stress relaxation. It is thus more realistic to assume that some stress relaxation due to the diffusion takes place during the high temperature regime. If T = 1500°C is considered as a threshold temperature, T_{th}, above which the stress relaxation due to the diffusion can occur, then T_P must be set equal to 1500°C in the elastic analysis of the thermal residual stress. For T_P = 1500°C, the predicted value of K_c/K_m = 1.43. The toughening effect based on T_P = 1500°C still constitutes the major portion of the observed toughness increase. The threshold temperature T_{th} is, however, difficult to determine since the creep (diffusion) behavior is a continuous function of temperature and time.

T_{th} of metal matrix composites can be estimated by *in situ* transmission electron microscopy (TEM) study[30] as the temperature, at which the dislocations start to appear in the matrix close to the matrix-filler interface during the cool down process. Such an *in situ* TEM study of a ceramic composite is difficult to conduct since T_{th} is too high for heating stage device within a TEM. In addition, the generation (punching) of the dislocations from the matrix-filler interface due to the CTE mismatch[31] is unlikely due to high friction stress of the ceramics matrix.

It was assumed in the present model that the crack propagation path over a number of tensile regions, each surrounding a particulate, is self-similar despite the locally wavy fracture surface. Figure 13(a) shows a typical BEI photo of a crack propagating in a TiB_2 particulate-reinforced/SiC-matrix composite toward the right and Fig. 13(b) is a portion of Fig. 13(a) at higher magnification . It is noted in Fig. 13(b) that the dark regions on the crack path were occupied by TiB_2 particulates which fell off during polishing. Both figures indicate that the crack actually propagated from particulate to particulate located on the crack plane. Figures 14(a) and (b) are BEI photos of the fracture surface of the composite and monolithic SiC, respectively. A comparison between Figs. 14(a) and (b) reveals that the degree of the local waviness of these photos is the same except for the regions next to particulates. This secondary wavy surface which is associated with the particulates are probably due to the crack deflection proposed by Faber and Evans[3]. The toughening due to this crack deflection was evaluated as K_c/K_m = 1.14. By superposing the toughening due to crack deflection onto that due to compressive stress in the matrix, one can estimate the toughness ratio as

$$\frac{K_c}{K_m} = 1 + 0.14 + 0.52 = 1.66 \qquad (19)$$

The toughness ratio so estimated is close to the experimental value of $K_c/K_m = 1.77$.

The validity of the present model can be partially supported by the experimental results by Jenkins et al.[9] where the crack growth resistance, K_R, of TiB_2/SiC composite measured at various temperatures from room to 1400°C exhibited a decrease with increasing testing temperature. Toughening in the present model is proportional to the compressive thermal residual stress in the matrix, which in turn is proportional to the temperature change, $\Delta T = T_T - T_P$, where T_T is the testing temperature for measuring K_R. Hence, the higher testing temperatures result in smaller increase in K_R as observed by Jenkins et al.[9]

The effect of volume fraction of particulate, f_p, can be examined by looking at eqs. (7), (9) and (10). The thermal residual stress in the matrix $\langle\sigma\rangle_m$ is an increasing function of f_p, as shown by eqs. (7) and (9), and will influence linearly ΔK_I obtained by eq. (10). On the other hand, the average interparticulate spacing, λ, is proportional to $1/\sqrt{f_p}$[31]

$$\lambda = 1.085\ d/\sqrt{f_p} \qquad (20)$$

while ΔK_I is proportional to $\sqrt{\lambda - d}$, as shown by eq. (10). Using the average measured diameter of the particulates, $d = 3.06\ \mu m$, one can calculate the interparticulate distance, λ, by eq. (20), which yields $\lambda = 8.14\ \mu m$. This value of λ is smaller than the average of the measured interparticulate distances on 70 TiB_2 particulates, $\lambda = 11.1\ \mu m$. This discrepancy between the measured and that predicted by eq. (20) is attributed to some error involved in our measurement or the degree of approximation inherent in eq. (20). Non-uniform distribution of TiB_2 particulate also contributed to a larger measured λ is larger than that predicted by eq. (20). By combining the above effects, the toughness ratios, K_c/K_m, are computed for various values of f_p. The predicted results of the K_c/K_m versus f_p relation are shown as a solid curve in Fig. 15, with the experimental value at $f_p = 0.16$ shown as an open circle. Also shown in Fig. 15 are the prediction of K_R based on the crack deflection model by Faber and Evans for two cases of particulates distribution; uniform spacing (dash) and distributed spacing (dash-dot). It is clearly seen from Fig. 15 that the present model can predict the observed toughness increase better than the crack deflection model and it can account for the major toughening of a composite. It follows from Fig. 15 that the crack growth rate ratio of the composite to the monolithic matrix increases with f_p. The rate of increase in K_c/K_m is, however, not linear with f_p but decreases with increase in f_p. This f_p dependence of the fracture toughness ratio has also been observed by other investigators.[6,33] As f_p increases to higher values, for example, in excess of 0.5, the present model fails to predict the correct trend of the K_c/K_m versus f_p relation. At such high volume fractions, many particulates come in contact and form large clusters. The microstructure of these clusters differs from that of the present model, as shown in Fig. 10. Thus, the K_c/K_m ratio would be saturated, or even start to decrease at higher volume fractions. Endo et al.[33] have indeed observed such a trend with

several non-oxide particulates-reinforced/SiC-matrix composite systems. Figure 16 shows the K_{IC} versus f_p relation of TiC particulate/SiC matrix composite.

The present model predicts high tensile stress in TiB_2 particulate at room temperature as per eq. (13). If this high tensile stress $\langle\sigma\rangle_p$ exceeds the bonding strength of the matrix-particulate interface, σ_b, then the interface will be debonded. It seems appropriate to assume that the interfacial bonding strength varies from particulate to particulate. Thus, some particulates with $\sigma_b \leq \langle\sigma\rangle_p$ would become debonded voids where the debonded interface cannot transfer stress except for compressive stress. It is, however, difficult to determine the percentage of such particulates with weak interface, but one can obtain a rough estimate of the percentage by observing the percentage of TiB_2 particulates that would fall out from the specimen during the polishing. If the debonded voids so nucleated are also counted, then the volume fraction of voids, f_v, increases as the fraction of TiB_2 particulates with weak interface increases. The effect of f_v on K_R can be studied by calculating the average compressive stress in the matrix $\langle\sigma\rangle_m$ using eqs. (5) and (6). The solid curve in Fig. 17 shows the results of $\langle\sigma\rangle_m$ as a function of f_v by assuming that voids are nucleated only from TiB_2 particulates, i.e., $f_v + f_p = 0.16$. $\langle\sigma\rangle_m$ is found to decrease with f_v and becomes zero when all the TiB_2 particulates are changed to voids. Thus the voids nucleate as a result of the debonding of the matrix-particulate interface would reduce the toughness of a particulate composite. On the other hand, if we assume that the voids are induced as a result of the processing (sintering and cool down process), and the matrix-particulate interfaces are bonded, then f_v dependence of $\langle\sigma\rangle_m$, as shown by the dashed curve in Fig. 17, has the opposite trend to the above case. Namely, $\langle\sigma\rangle_m$ increases gradually with the increase in f_v, thus contributing to the toughness of a particulate composite, although the increase in the toughness is modest. The values of f_v, however, are usually small as in the present case ($f_v = 0.016$). Thus the effect of voids on K_R can be considered minimal.

The effect of cyclic loading on K_R of a TiB_2 particulate-reinforced/SiC-matrix is obvious from Fig. 9. Namely, the cyclic loading defined by Fig. 8 tends to reduce the value of K_R by about 0.7 $m\sqrt{Pa}$. This reduction in K_R can be explained as follows: the cyclic loading modifies the local stress field including the residual thermal stress, resulting in the lower compressive stress in the matrix. Thus a crack front is subjected to such a modified thermal stress field during the loading process following the preceding unloading, leading to the reduction in the toughness. This modified thermal stress field would not occur in the monolithic SiC due to the lack of TiB_2 particulates.

IV. Conclusion

Increase in the K_R of the composite over the unreinforced matrix is attributed to new analytical model based on the compressive thermal residual stress in the matrix in a particulate reinforced ceramic matrix composite. The K_R predicted by this model agrees with the experimental value better than an existing model.

V. Acknowledgements

The present work was supported by ONR contract (N00014–87–K–03260) where Dr. Y. Rajapakse is the Scientific Program Officer. Discussion with Professor T. Mori of the Tokyo Institute of Technology and Professor Y. Sumi of Yokohama National University are greatly appreciated. The authors also wish to thank Dr. S. Seshadari, British Petroleum Engineering Material Company for providing the TiB_2-particulate/SiC-matrix composite specimens.

References

1. F.F. Lange, Phil. Mag. 22, 983–82 (1970).

2. A.G. Evans, Phil. Mag., 26, 1327–1344 (1972).

3. K.T. Faber and A.G. Evans, Acta Metall. 31 [4], 565–576, (1983).

4. B. Budiansky, J.C. Amazigo and A.G. Evans, J. Mech. Phys. Solids, 36, 167–187, (1988).

5. G.C. Wei and P.F. Becher, J. Am. Ceram. Soc., 67, 571–574 (1984).

6. C.H. McMurtry, W.D.G. Boecker, S.G. Seshadri, J.S. Zanghi and J.E. Garnier, Am. Ceram. Soc. Bull., 66 [2], 325–329 (1987)

7. S.J. Buljan, J.G. Baldoni and M.L. Huckabee, Am. Ceram. Soc. Bull., 66 [2], 347–352 (1987).

8. M.A. Janney, Am. Ceram. Soc. Bull. 66 [2], 322–324 (1987).

9. M.G. Jenkins, J.A. Salem, and S.G. Seshadri, NASA Tech. Memo 100967, June 1988.

10. P.L. Swanson, C.J. Fairbanks, B.R. Lawn, Y.W. Mai and B.J. Hockey, J. Am. Ceram. Soc., 70 [4] 279–289 (1987).

11. T. M[illegible] and T. Mura, Mech. of Mater., 3, 193–198, (1984).

12. D.[illegible]arshall, B.N. Cox and A.G. Evans, 33, 2013–2021 (1985).

13. [illegible] Budi[illegible]sky, J. W. Hutchison and A.G. Evans, J. Mech. Phys. Solids, 34, 167–189 (1988).

14. M. Hori and S. Nemat-Nasser, Mech. of Mater., 6, 245–269 (1987).

15. L.R.F. Rose, J. Mech. Phys. Solids, 35, 383–405 (1987).

16. A. Taylor and R.M. Jones, "Silicon Carbide: A High Temperature Semiconductor," edited by J.R. O'Connor and J. Smiltens, Pergamon Press, p. 151 (1960).

17. "Thermophysical Properties of High Temperature Solid Materials," edited by Y.S. Touloukian, MacMillan Company, New York, 6, 244 (1973).

18. "Determining Volume Fraction by Systematic Manual Point Count," ANS/ASTM E562–76, 594–603 (1980).

19. A.S. Kobayashi, "Hybrid Experimental-Numerical Analysis," chap. 2, in *Handbook on Experimental Mechanics*, edited by A.S. Kobayashi, Prentice Hall, Englewood Cliffs (1987).

20. D. Post, "Moire Interfermoetry," Chap. 5 in *Handbook on Experimental Mechanics*, edited by A.S. Kobayashi, Prentice Hall, Englewood Cliffs (1987).

21. H.F. Kirkwood and M.E. Prado, ASTM STP 601, 267–273 (1976).

22. J.D. Eshelby, Proc. R. Soc. London, A241, 376–396 (1957).

23. T. Mori and K. Tanaka, Acta Metall., 21, 571–574 (1973).

24. T. Mura, Micromechanics of Defects in Solids, 2d ed., Martinus Nijhoff, Publishers, Chap. 7 (1987).

25. M. Taya and R.J. Arsenault, Metal Matrix Composites: Thermomechanical Behavior, Pergamon Press, Chap. 3 (1989).

26. Y. Takao and M. Taya, J. Appl. Mech., 52, 806–810 (1985).

27. K. Wakashima, Y. Suzuki and S. Umekawa, J. Comp. Mater., 13, 288–302 (1979).

28. H. Tada, P.C. Paris and G.R. Irwin, The Stress Analysis of Cracks, Handbook, Del Research Corp, p. 3.7 (1973).

29. P.M. Sargent and M.F. Ashby, Scripta Metal., 17, 951–957 (1983).

30. M. Vogelsang, R.M. Fisher and R.J. Arsenault, Metall. Trans., 17A, 379–389 (1986).

31. M. Taya and T. Mori, *Acta Metall.* 35, 155-162 (1987).

32. G. Leroy, J.D. Embury, G. Edwards and M.F. Ashby, Acta Metall., 29, 1509–1522 (1981).

33. H. Endo, M. Ueki and H. Kubo, presented at the World Mater. Congress 1988, Session VIII: Ceramic Matrix Composites, Sept. 1988, Chicago.

Table 1 Material Properties of SiC and TiB_2

Properties	Unit	SiC	TiB_2
Crystal structure		hexagonal	hexagonal
Specific gravity	g/cm^3	3.21	4.52
Melting point	°C	2540*	2790
Young's modulus	GPa	410	531
Poisson's ratio	1	0.19	0.28
Average size	μm	grain size 3	2.06***
Volume fraction		0.84	0.16
CTE**	$10^{-6}/°C$	4.02	4.6

* Degassing temperature

** These CTE values taken from ref. 6 are averages over room temperature~700°C range, and are not accurate. The accurate CTE values of SiC and TiB_2 200~2200K[16,17] are given in Fig. 1.

***This value, which is taken from ref. 6, is smaller than the average value that we have measured. This is discussed later.

Appendix: The Formulation for the Thermal Residual Stresses

Referring to Fig. 10(b), the internal elastic stress field in domain Ω_1 (particulates) and Ω_2 (voids) are denoted by $\underset{\sim}{\sigma}^1$ and $\underset{\sim}{\sigma}^2$, respectively, which are:

$$\underset{\sim}{\sigma}^1 = \mathbf{C}^p \cdot (\bar{\boldsymbol{\varepsilon}} + \boldsymbol{\varepsilon}^1 - \underset{\sim}{\varepsilon}^1) \quad \text{in } \Omega_1 \tag{A1}$$

$$\underset{\sim}{\sigma}^2 = \mathbf{C}^v \cdot (\bar{\boldsymbol{\varepsilon}} + \boldsymbol{\varepsilon}^2 - \underset{\sim}{\varepsilon}^2) \quad \text{in } \Omega_2 \tag{A2}$$

where the bold face letters and those with subscripted tildas denote tensorial quantities, $\mathbf{C}^p$ and $\mathbf{C}^v$ are the stiffness tensor (of rank 4) of the particulate and void, respectively, $\boldsymbol{\varepsilon}^1$ and $\boldsymbol{\varepsilon}^2$ are the strain disturbed by Ω_1 and Ω_2, respectively, and $\bar{\boldsymbol{\varepsilon}}$ is the average strain in the matrix, and related to the average stress in the matrix $\langle\sigma\rangle_m$ as

$$\langle\underset{\sim}{\sigma}\rangle_m = \mathbf{C}^m \cdot \bar{\boldsymbol{\varepsilon}} \tag{A3}$$

The dots used in the above equations denote inner product between tensors. Following Eshelby,[22] Fig. 10(b) can be further reduced to Fig. 10(c) where two inhomogeneities, particulates and voids, are now replaced by two inclusions. An inclusion is a domain surrounded by the matrix and possesses the same properties as the matrix and also an eigenstrain $\boldsymbol{\varepsilon}^*$ which is an inelastic strain.[24] Thus Equations (A1) and (A2), which are formulated based on Fig. 10(b), are now reduced to the following, Fig. 10(c):

$$\underset{\sim}{\sigma}^1 = \mathbf{C}^m \cdot (\bar{\boldsymbol{\varepsilon}} + \boldsymbol{\varepsilon}^1 - \boldsymbol{\varepsilon}^{*1}) \quad \text{in } \Omega_1 \tag{A4}$$

$$\underset{\sim}{\sigma}^2 = \mathbf{C}^m \cdot (\bar{\boldsymbol{\varepsilon}} + \boldsymbol{\varepsilon}^2 - \boldsymbol{\varepsilon}^{*2}) \quad \text{in } \Omega_2 \tag{A5}$$

Here eqs. (A4) and (A5) are valid for the entire composite domain, D, if the eigenstrains, $\boldsymbol{\varepsilon}^{*1}$ and $\boldsymbol{\varepsilon}^{*2}$, are defined as zero in the domain outside Ω_1 and Ω_2, respectively. Noting that the integration of the stress field $\underset{\sim}{\sigma}^1$ and $\underset{\sim}{\sigma}^2$ over D vanishes:

$$\int_D \underset{\sim}{\sigma}\, dv = 0 \tag{A6}$$

we obtain

$$\bar{\boldsymbol{\varepsilon}} = -f_p\,(\boldsymbol{\varepsilon}^1 - \boldsymbol{\varepsilon}^{*1}) - f_v\,(\boldsymbol{\varepsilon}^2 - \boldsymbol{\varepsilon}^{*2}) \tag{A7}$$

where f_p and f_v are the volume fraction of the particulate and void, respectively. The strain field, $\boldsymbol{e}^1$ and $\boldsymbol{e}^2$, in the inclusions, are related to the corresponding eigenstrain, $\boldsymbol{e}^{*1}$ and $\boldsymbol{e}^{*2}$, respectively, by the Eshelby's tensor **S**:

$$\boldsymbol{e}^1 = \mathbf{S} \cdot \boldsymbol{e}^{*1} \tag{A8}$$

$$\boldsymbol{e}^2 = \mathbf{S} \cdot \boldsymbol{e}^{*2} \tag{A9}$$

Eshelby's tensor (of rank 4) for an isotropic matrix is a function of the Poisson ratio of the matrix, ν_m, and the geometry of Ω.[22,24]

By equating eqs. (A1) and (A2) to eqs. (A4) and (A5), using $\mathbf{C}^v = 0$ due to voids, and eqs. (A7) through (A9), we arrive at:

$$\mathbf{C}^p \cdot [(1-f_p)\mathbf{S} \cdot \boldsymbol{e}^{*1} + f_p \boldsymbol{e}^{*1} - f_v (\mathbf{S} \cdot \boldsymbol{e}^{*2} - \boldsymbol{e}^{*2}) - \underset{\sim}{\varepsilon}^{*1}] =$$

$$\mathbf{C}^m \cdot [(1-f_p)(\mathbf{S} \cdot \boldsymbol{e}^{*1} - \boldsymbol{e}^{*1}) - f_v (\mathbf{S} \cdot \boldsymbol{e}^{*2} - \boldsymbol{e}^{*2})] \tag{A10}$$

$$-f_p \boldsymbol{e}^{*1} + (1 - f_v)\boldsymbol{e}^{*2} = 0 \tag{A11}$$

where the isotropic stiffness tensors, $\mathbf{C}^m$ and $\mathbf{C}^p$, and misfit strain $\underset{\sim}{\varepsilon}^{*1}$ are given in index form as:

$$C^J_{ijkl} = \lambda_J \delta_{ij}\delta_{kl} + \mu_J(\delta_{ik}\delta_{jl} + \delta_{il}\delta_{kj}), \quad J = m \text{ or } p \tag{A12}$$

$$\alpha^{*1}_{ij} = \int_{T_P}^{T_R} (\alpha_p - \alpha_m)\, \delta_{ij}\, dT \tag{A13}$$

where δ_{ij} is the Kronecker's delta, λ_J and μ_J are Lamé constants of the J-th phase material ($J = m$ for the matrix, $J = p$ for the particulate), α_m and α_p are the CTE of the matrix and particulate, respectively, and T_R and T_P are the room and processing temperatures, respectively.

The problem, which is illustrated Fig. 10(c), gives rise to isotropic state since the particulate reinforcement and the CTE mismatch strain are dilatational. Hence only one independent component for each unknown eigenstrain in eqs. (A10) and (A11) exists. Eshelby's tensor components required for solving eqs. (A10) and (A11), thus are:

$$S_{1111} = S_{2222} = S_{3333} = \frac{7 - 5\nu_m}{15(1 - \nu_m)}$$

$$S_{1122} = S_{2233} = S_{3311} = S_{1133} = S_{3322} = S_{2211} = \frac{5\nu_m - 1}{15(1 - \nu_m)} \tag{A14}$$

After substituting eq. (A14) into eqs. (A10) and (A11) and eliminating e^{*2}, we can solve for e_1^* ($= e_{11}^{*1} = e_{22}^{*1} = e_{33}^{*1}$)

$$e_1^* = \frac{3\beta\alpha_1^*}{\left[\left\{1 - \frac{f_p}{(1-f_v)}\right\}(\beta+2)\left(\frac{1+\nu_m}{1-\nu_m}\right) + \frac{3\beta f_p}{(1-f_v)}\right]} \tag{A15}$$

where

$$\beta = \frac{3\lambda_p + 2\mu_p}{2\mu_m} = \frac{(1+\nu_m)}{(1-2\nu_p)}\left(\frac{E_p}{E_m}\right) \tag{A16}$$

The eigenstrain in Ω_2, e^{*2} (i.e. $e_2^* = e_{11}^{*2} = e_{22}^{*2} = e_{33}^{*2}$) can be obtained from eq. (A11) once e_1^* is solved.

The average stresses in the particulate $\langle\sigma\rangle_p$ and in the matrix $\langle\sigma\rangle_m$ are related to each other by eq. (A6).

$$f_p\langle\sigma\rangle_p + (1-f_p-f_v)\langle\sigma\rangle_m = 0 \tag{A17}$$

where the stress in a void being zero was used, and $\langle\sigma\rangle_J$ with J = m (matrix) or p (particulate) denote an isotropic component, not tensor, $\underset{\sim}{\sigma}$

The average stress in the particulate $\langle\sigma\rangle_p$ can be calculated from eqs. (A4) and (A7) through (A9) once e_1^* and e_2^* are solved, and is given by

$$\frac{\langle\sigma\rangle_p}{E_m} = \frac{-2(1-f_p-f_v)\beta\alpha_1^*}{(1-f_v)\left[\left\{1-\frac{f_p}{1-f_v}\right\}(\beta+2)(1+\nu_m) + \frac{3\beta f_p(1-\nu_m)}{(1-f_v)}\right]} \tag{A18}$$

The average stress in the matrix $\langle\sigma\rangle_m$ then is obtained from eqs. (A17) and (A18)

$$\frac{\langle\sigma\rangle_m}{E_m} = \frac{2f_p\beta\alpha_1^*}{(1-f_v)\left[\left\{1-\frac{f_p}{1-f_v}\right\}(\beta+2)(1+\nu_m) + \frac{3\beta f_p(1-\nu_m)}{(1-f_v)}\right]} \tag{A19}$$

Eqs. (A18) and (A19) provide the average thermal residual stresses in a particle composite with voids due to CTE mismatch. When the composite does not contain voids, $f_v = 0$, eqs. (A18) and (A19) are simplified to

$$\frac{\langle\sigma\rangle_p}{E_m} = \frac{-2(1-f_p)\beta\dot{\alpha_1}}{\left[(1-f_p)(\beta+2)(1+\nu_m) + 3\beta f_p(1-\nu_m)\right]} \tag{A20}$$

and

$$\frac{\langle\sigma\rangle_m}{E_m} = \frac{2f_p\beta\dot{\alpha_1}}{\left[(1-f_p)(\beta+2)(1+\nu_m) + 3\beta f_p(1-\nu_m)\right]} \tag{A21}$$

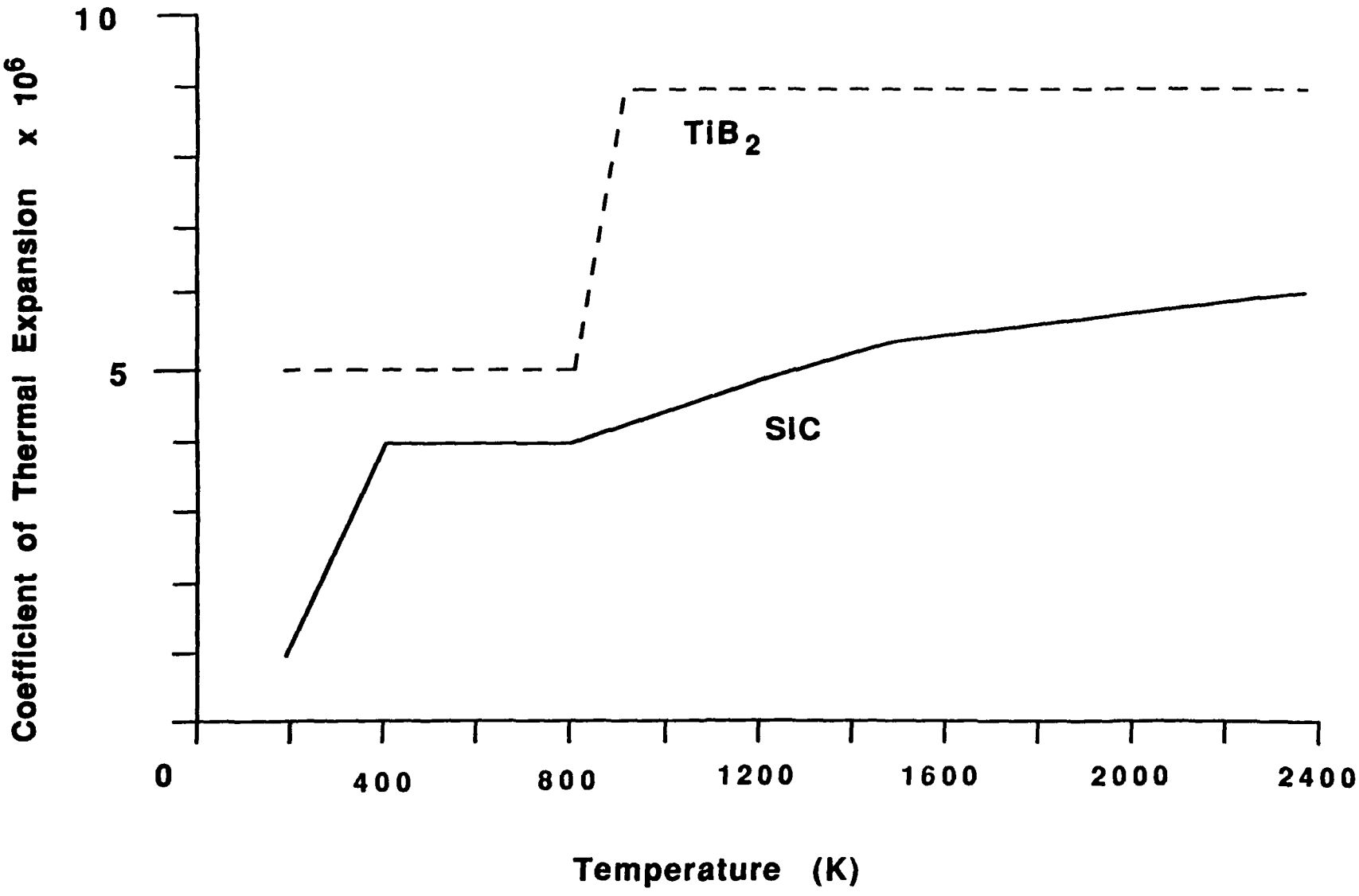

Fig. 1 Coefficients of thermal expansion of TiB_2 and α-SiC over the temperature range of 300–2400K.

(a)

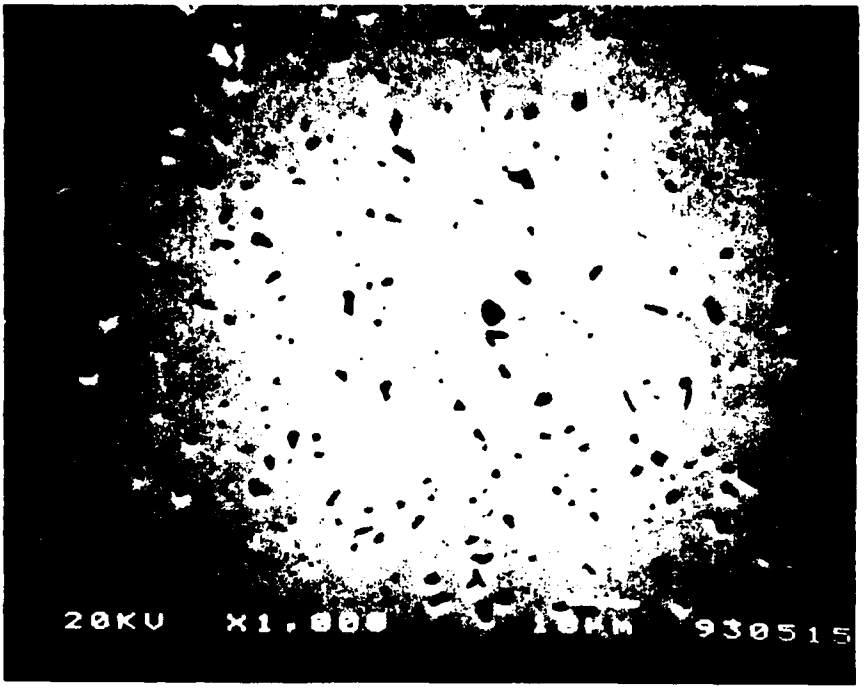

(b)

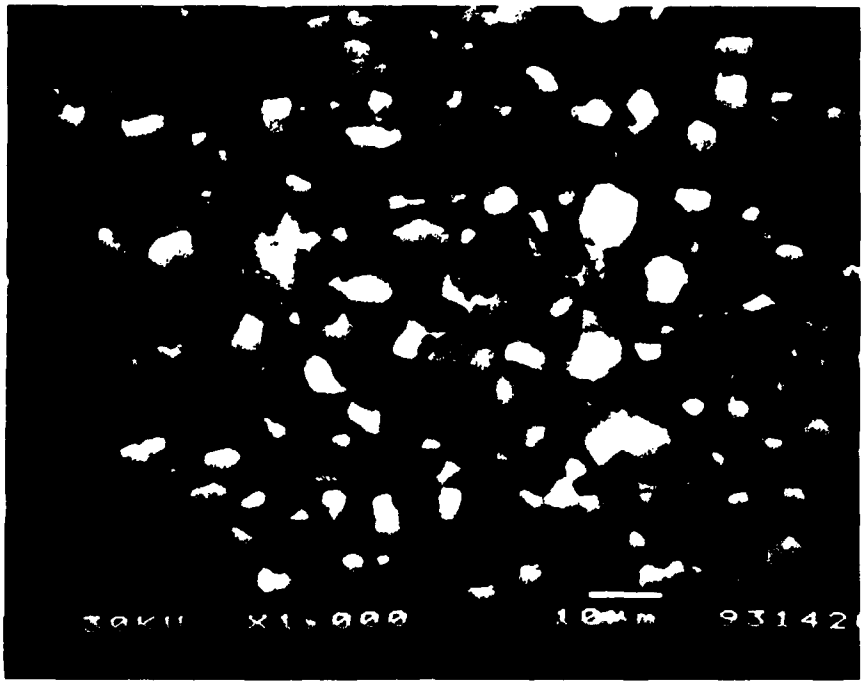

Fig. 2 Typical backscattered electron image of: (a) as-processed SiC; and (b) TiB_2/SiC composite.

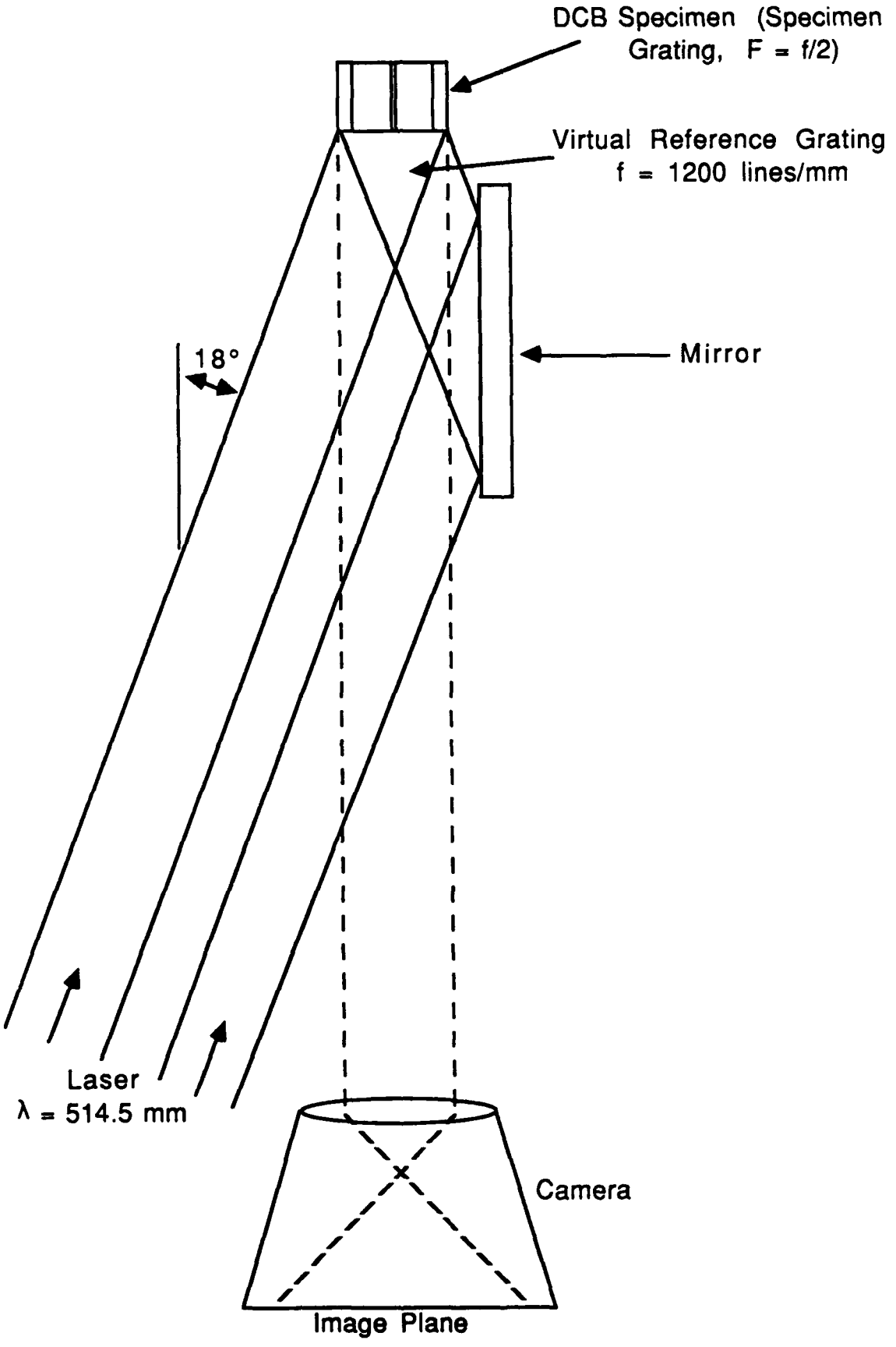

Fig. 3 Moire interferometry setup

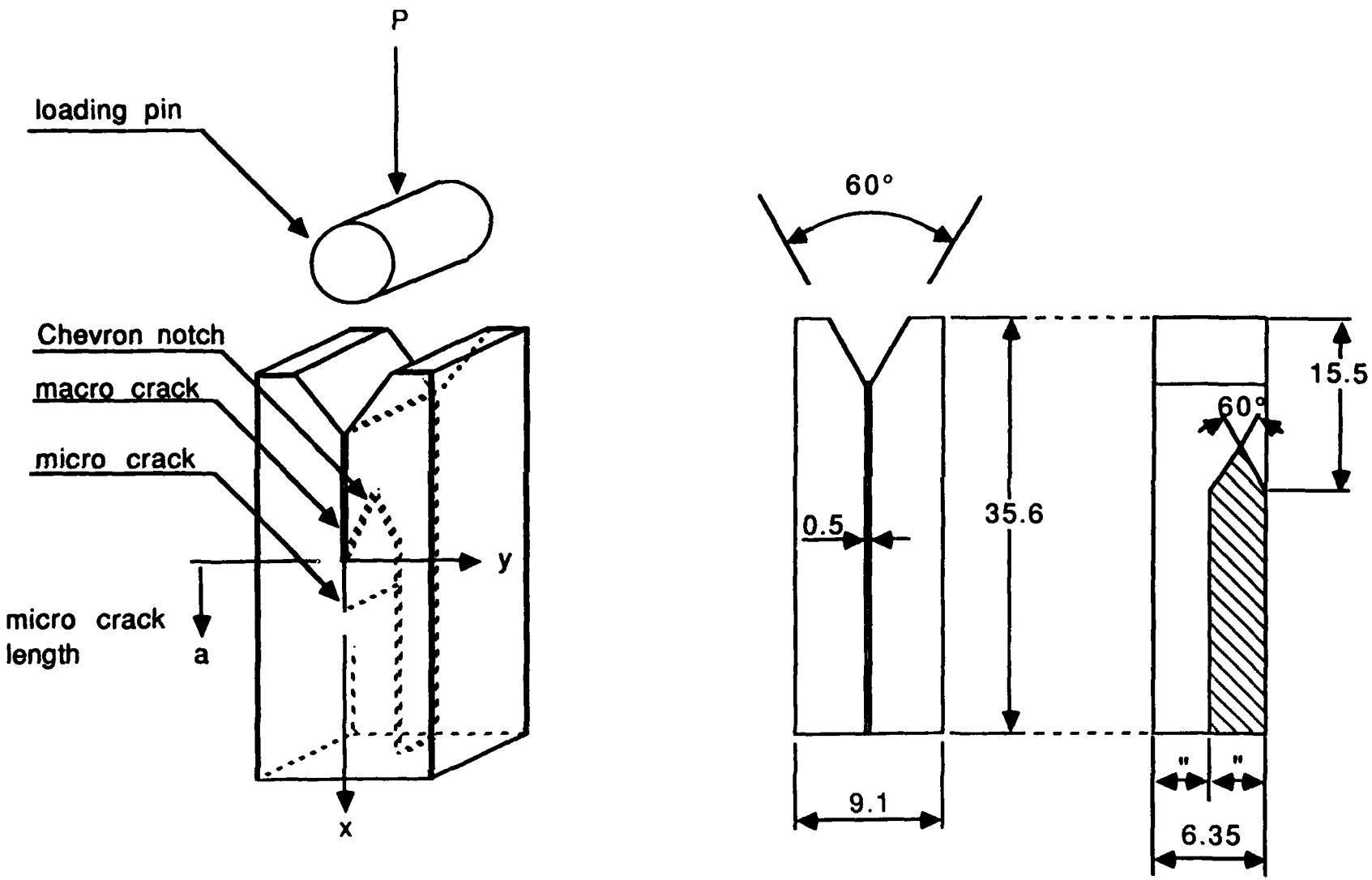

Fig. 4 Wedge-loaded double cantilever beam (WL-DCB) specimen with chevron notch and loading pin. All dimensions in mm.

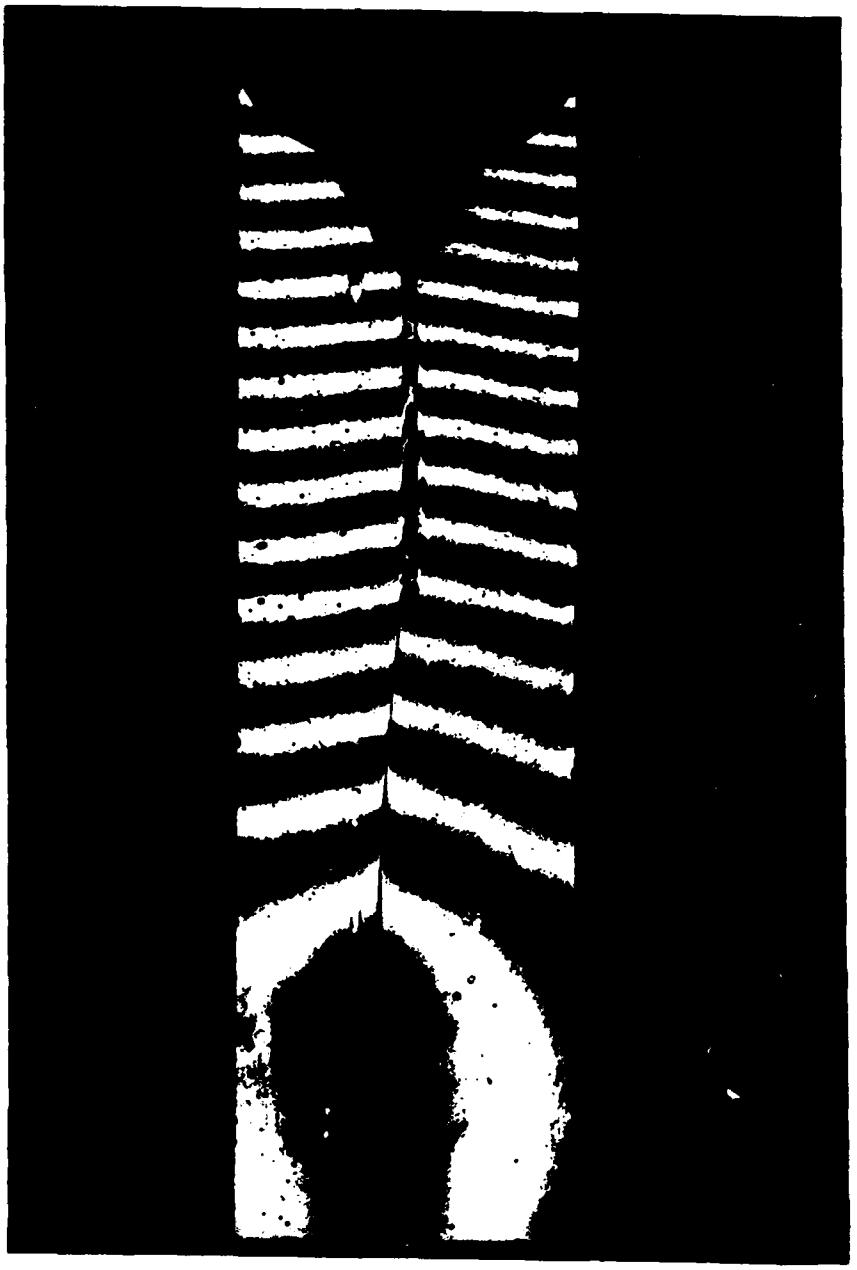

Fig. 5 A typical moire fringe pattern on a TiB_2/SiC composite specimen loaded to p = 65 N with the corresponding crack extension Δa = 9.6 mm.

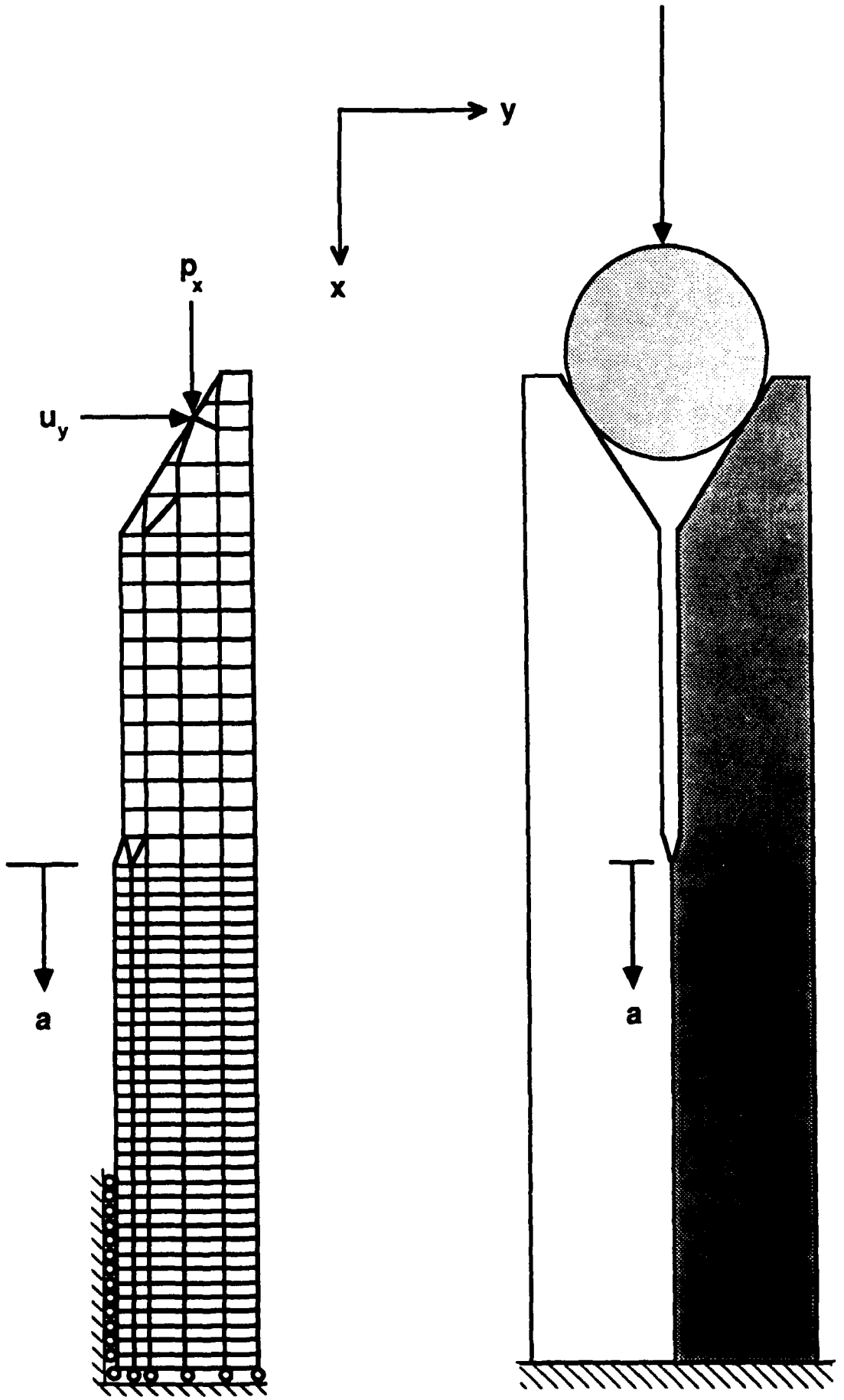

Fig. 6 2-D finite element analysis model with boundary conditions.

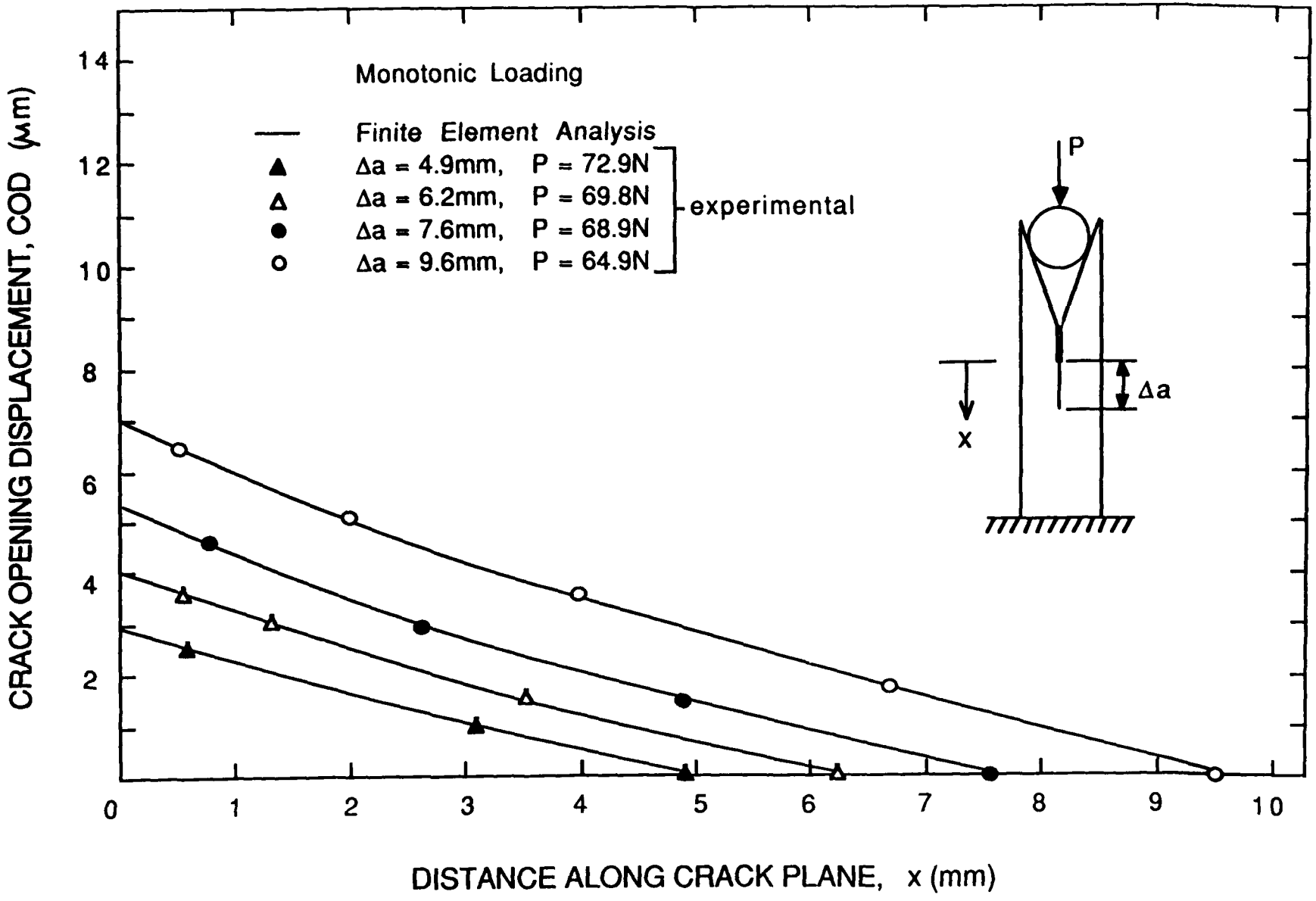

Fig. 7 COD along crack plane for various crack extensions; finite element analysis (solid curve) and experimental results (symbols).

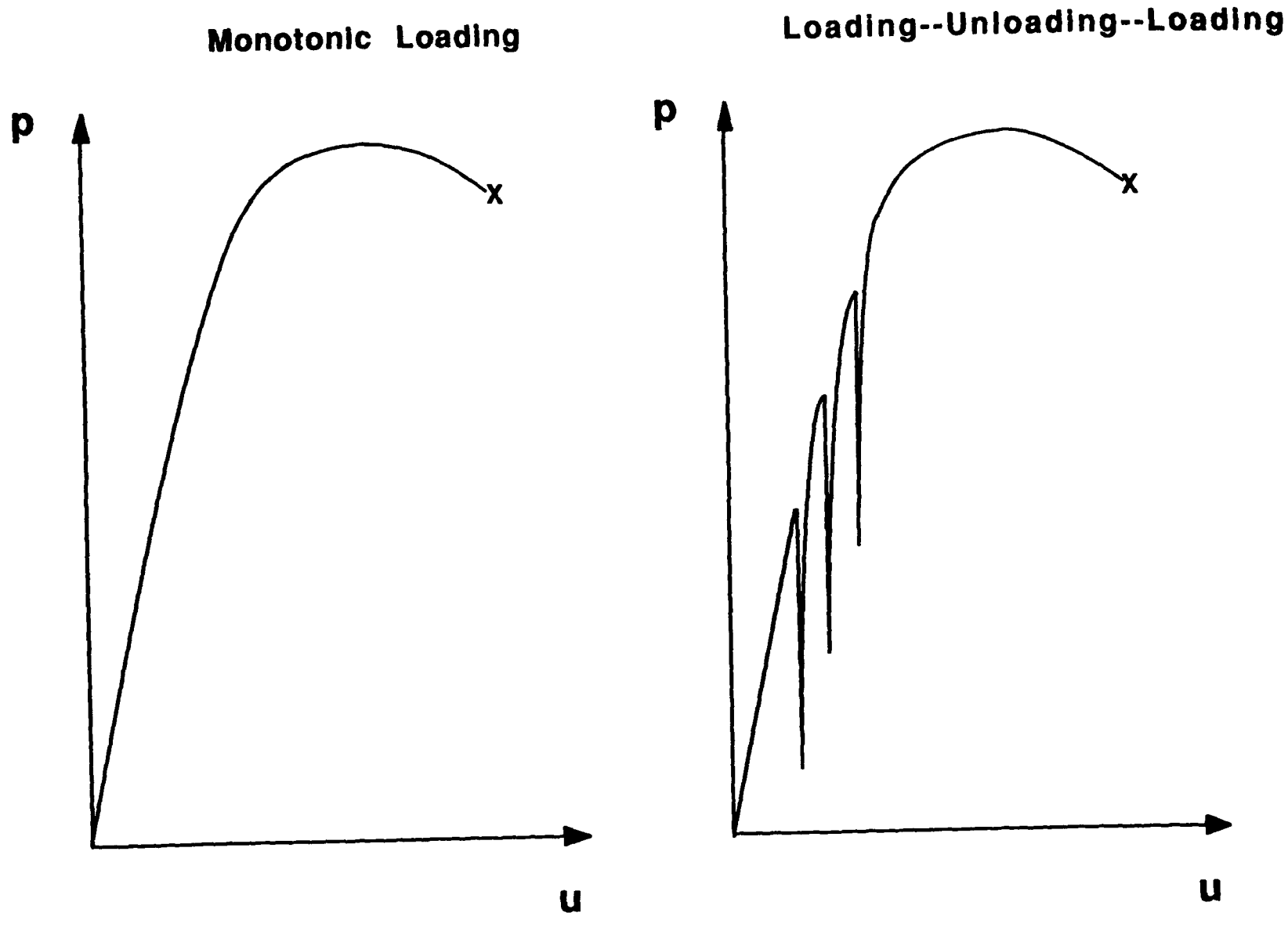

Fig. 8 Load (p) versus displacement (u) relations; (a) monotonic and (b) cyclic.

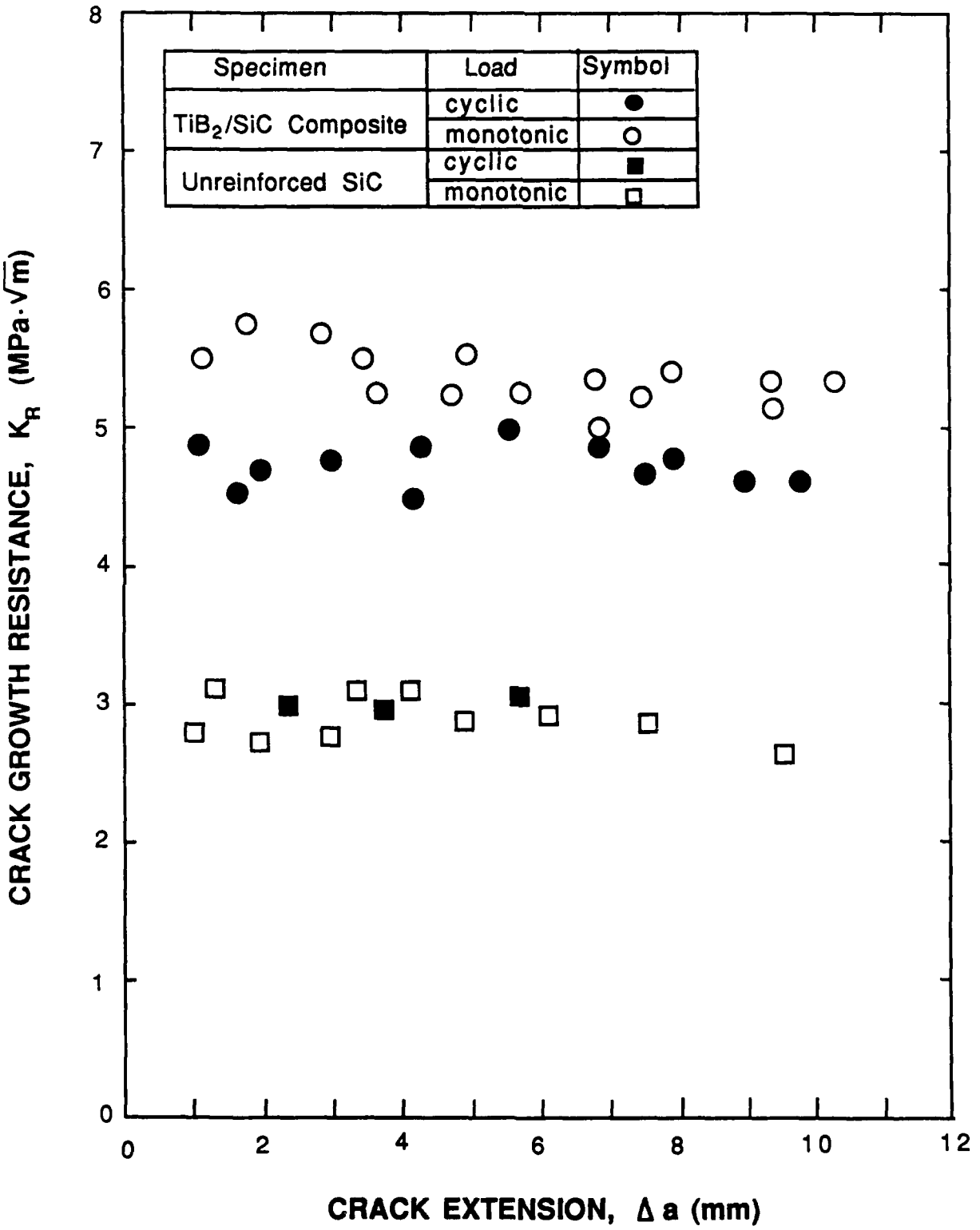

Fig. 9 Crack growth resistance, K_R versus crack extension, Δa, relations of the monolithic SiC (squares) and TiB_2/SiC composite (circles).

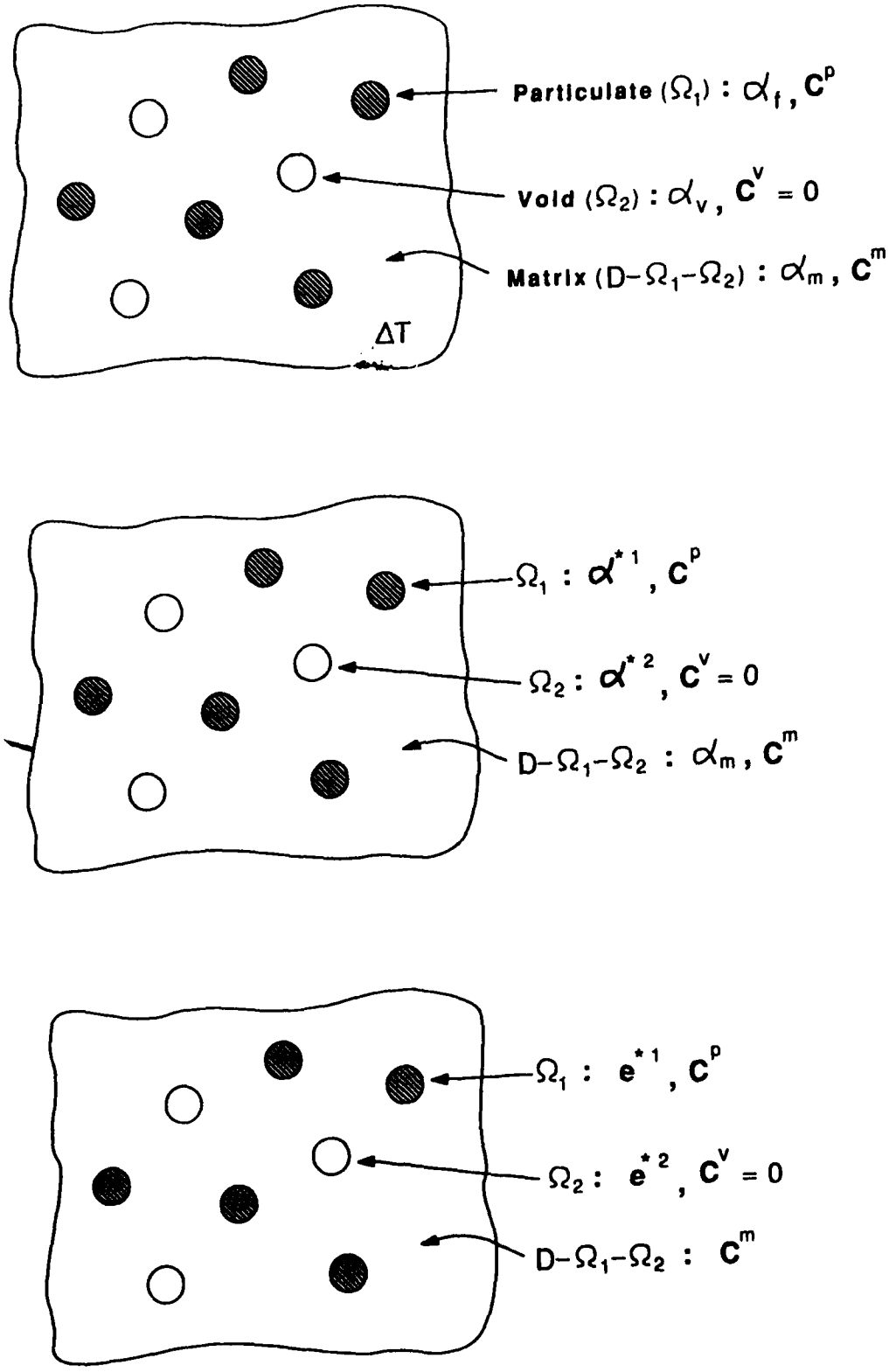

Fig. 10 Analytical model: (a) particulate reinforced composite with voids subjected to uniform temperature change ΔT; (b) two inhomogeneities with CTE misfit strains ε^{*1} in Ω_1 and ε^{*2} in Ω_2 embedded in the matrix $D-\Omega_1-\Omega_2$; and (c) converted to the Eshelby's inclusion problem.

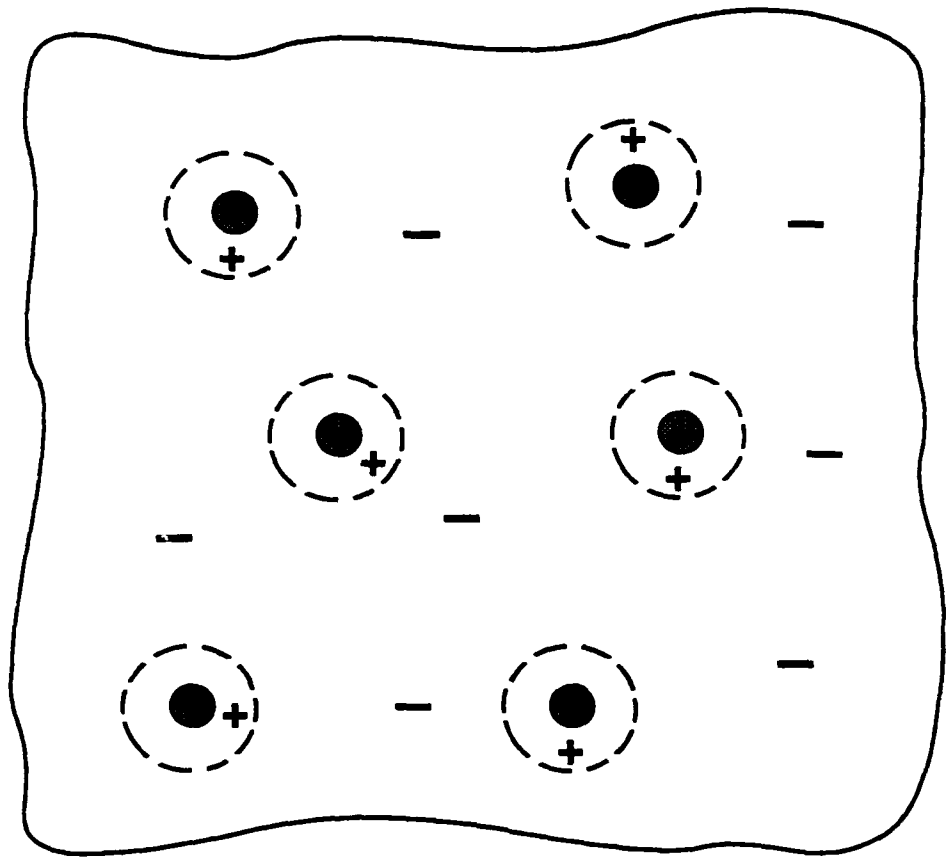

Fig. 11 Thermal residual stress field in a particulate-reinforced/ceramic-matrix composite.

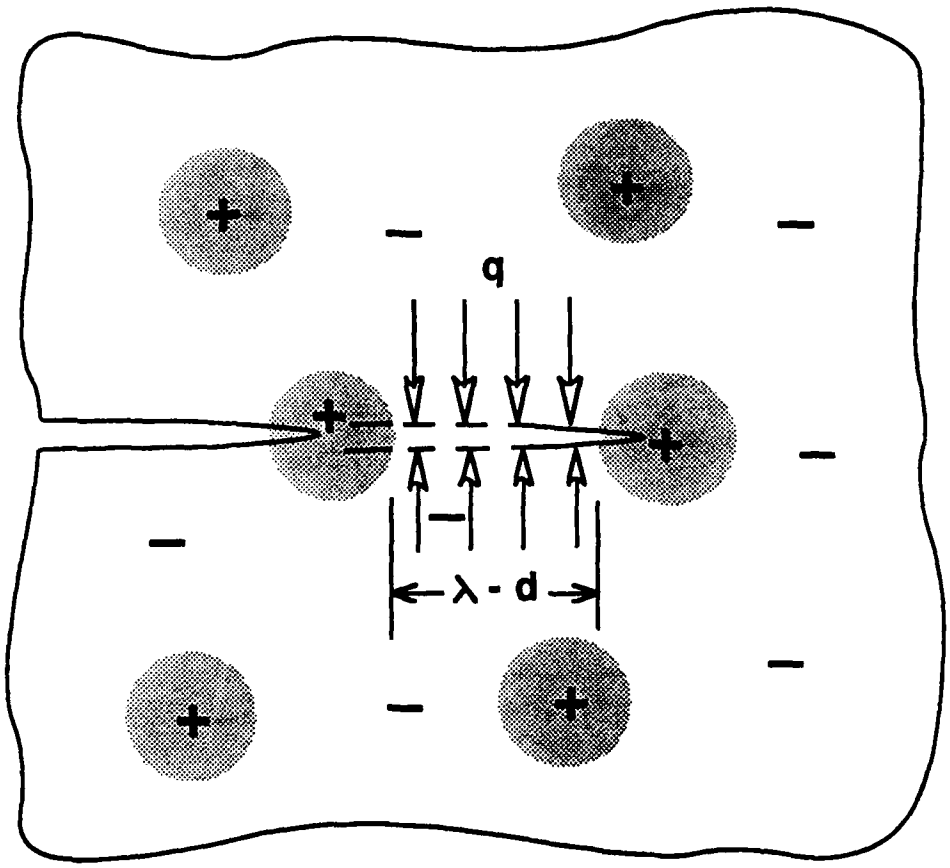

Fig. 12 Semi-infinite crack advances, λ, through matrix compressive region toward particulate tensile region.

(a)

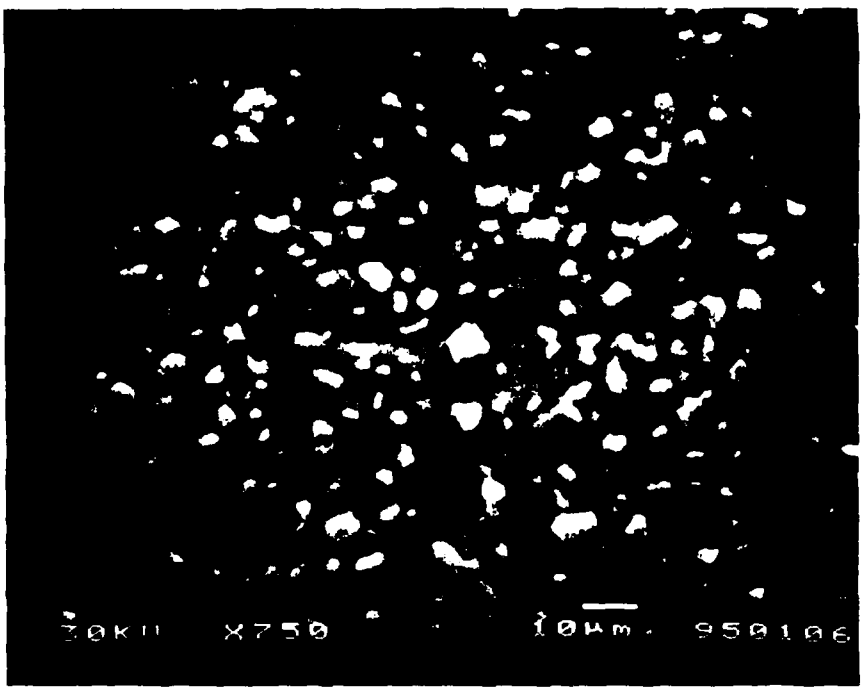

(b)

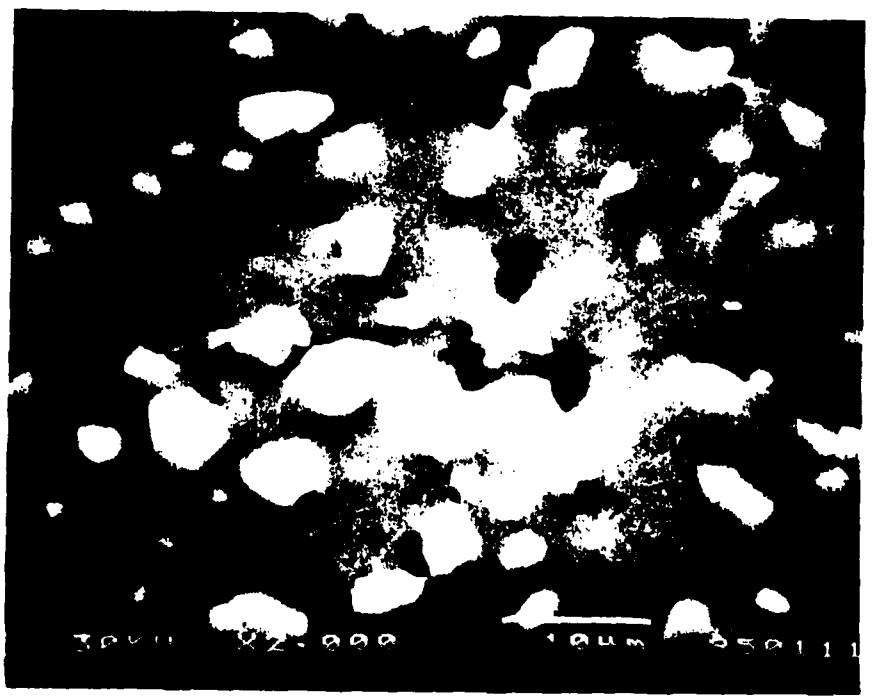

Fig. 13 (a) Backscattered electron image (BEI) of typical crack propagating path in a TiB_2 particulate-reinforced/SiC-matrix composite, (b) a segment of (a) at higher magnification.

(a)

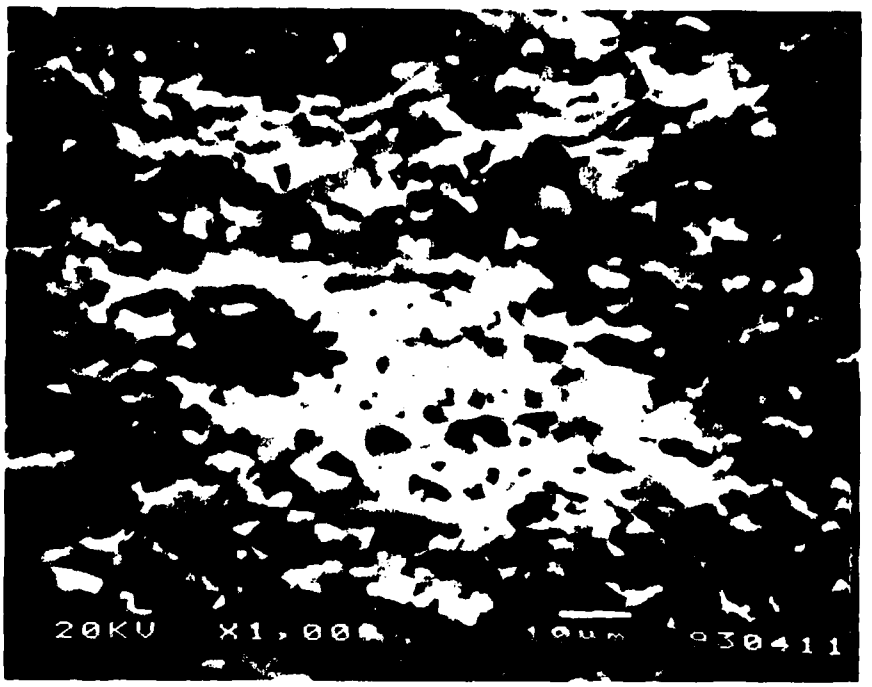

(b)

Fig. 14 BEI of fracture surface: (a) TiB_2/SiC composite; (b) monolithic SiC.

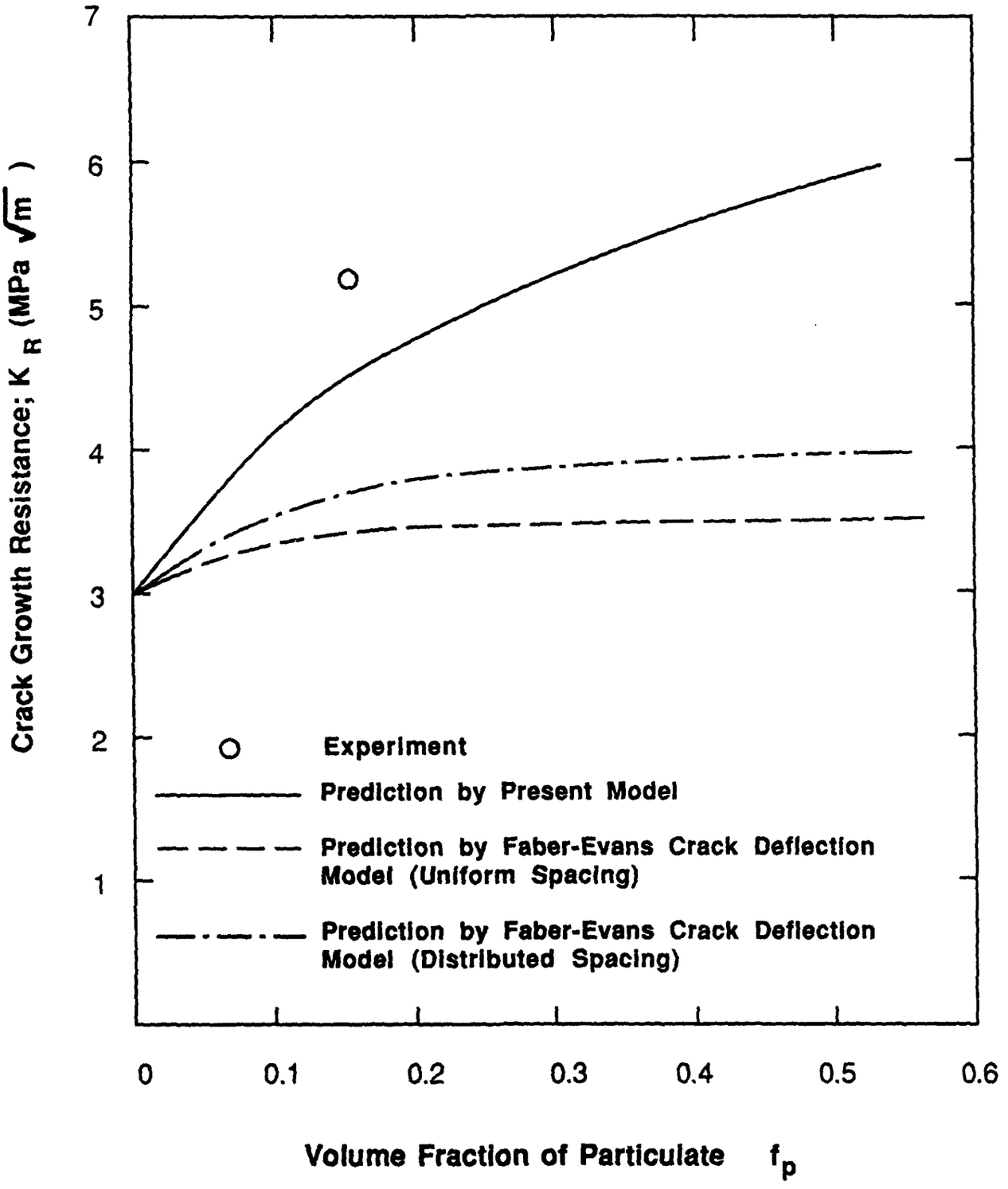

Fig. 15 The crack growth resistance ratio; TiB_2-particulate/SiC-matrix composite to the monolithic SiC, as a function of the volume fraction of TiB_2 particulates, f_p. Predictions based on the present model (solid curve) and Faber-Evans crack deflection model (dash and dash-dot curves), and the present experimental result at f_p = 0.16 (open circle).

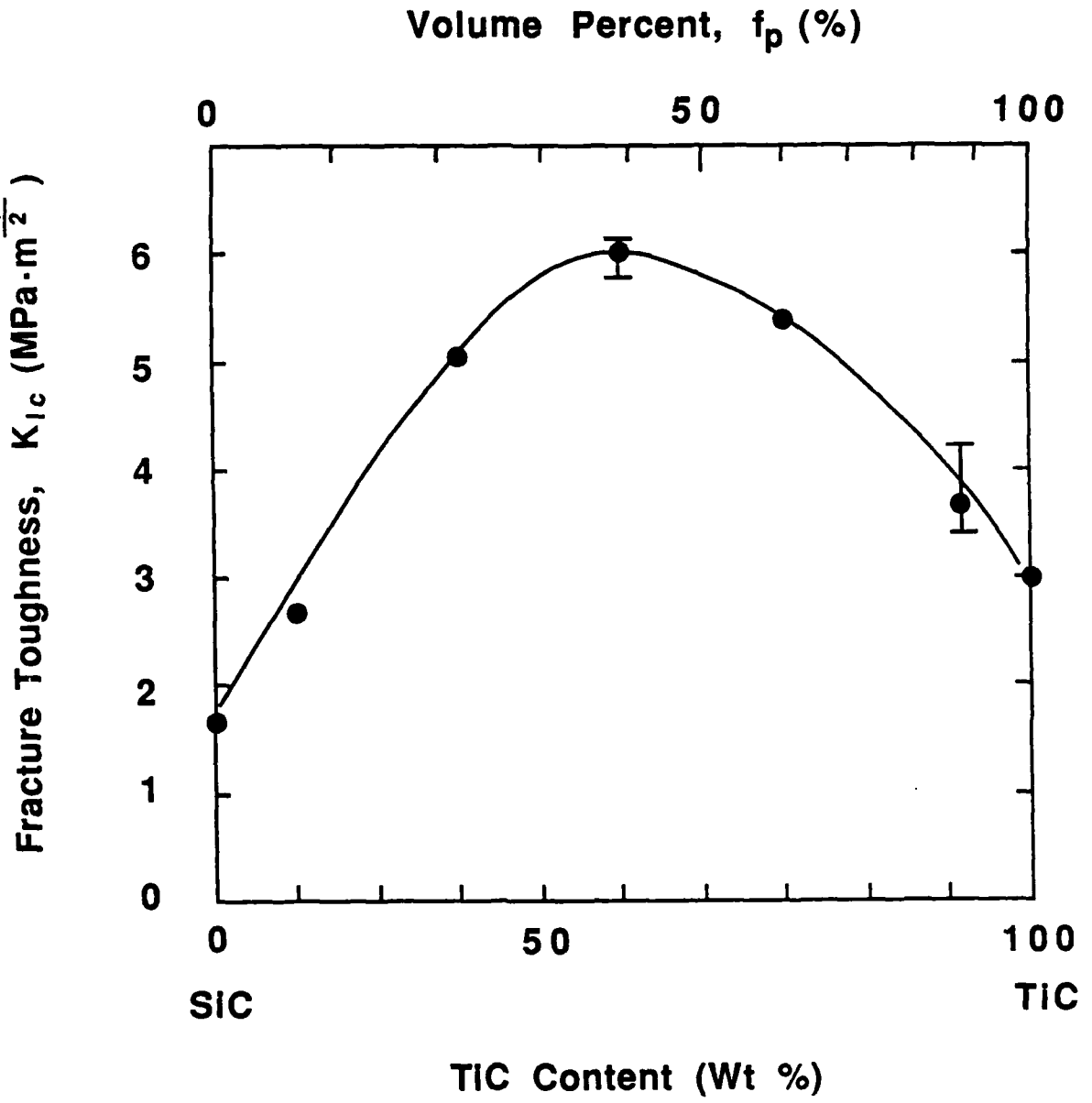

Fig. 16 K_{IC} versus f_p relation of TiC-particulate/SiC-matrix composite.[33]

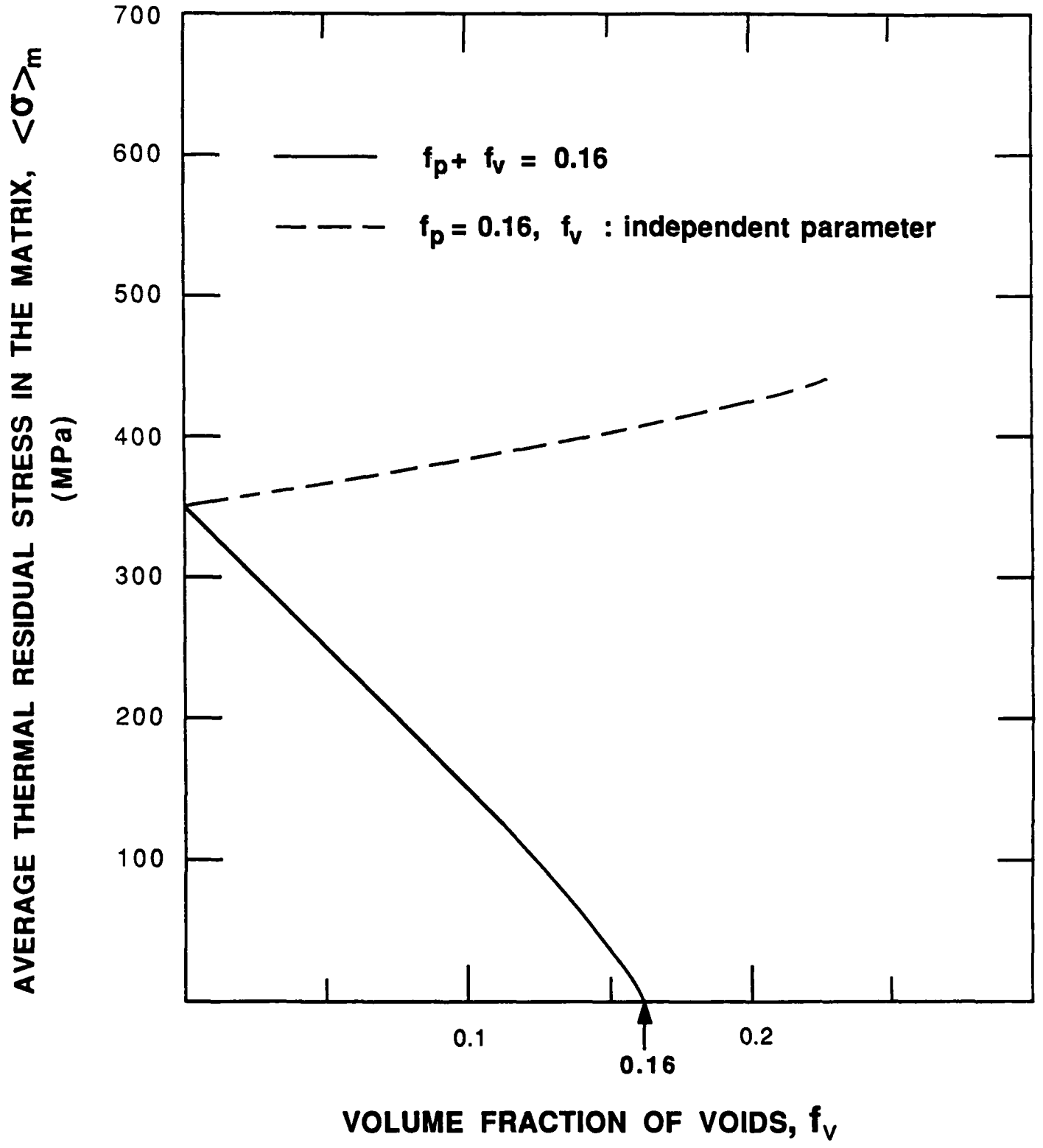

Fig. 17 $\langle\sigma\rangle_m$ as a function of volume fraction of voids, f_v. Predicted by eqs. (5) and (6).

Office of Naval Research
800 N Quincy Street
Arlington, VA 22217-5000
Attn: Code 11325M (4 copies)

Office of Naval Research
800 N Quincy Street
Arlington, VA 22217-5000
Attn: Code 1131

Defense Documentation Cntr
(4 copies)
Cameron Station
Alexandria, VA 02314

Naval Research Laboratory
Washington, DC 20375
Attn: Code 6000

Naval Research Laboratory
Washington, DC 20375
Attn: Code 6300

Naval Research Laboratory
Washington, DC 20375
Attn: Code 6380

Naval Research Laboratory
Washington, DC 20375
Attn: Code 5830

Naval Research Laboratory
Washington, DC 20375
Attn: Code 6390

Naval Research Laboratory
Washington, DC 20375
Attn: Code 2620

David W. Taylor Naval Ship
R & D Center
Annapolis, MD 21402
Attn: Code 28

David W. Taylor Naval Ship
R & D Center
Annapolis, MD 21402
Attn: Code 2812

David W. Taylor Naval Ship
R & D Center
Annapolis, MD 21402
Attn: Code 2814

David W. Taylor Naval Ship
R & D Center
Annapolis, MD 21402
Attn: Code 1700

David W. Taylor Naval Ship
R & D Center
Annapolis, MD 21402
Attn: Code 1720

David W. Taylor Naval Ship
R & D Center
Annapolis, MD 21402
Attn: Code 1720.4

Naval Air Development
Center
Warminster, PA 18974
Attn: Code 6043

Naval Air Development
Center
Warminster, PA 18974
Attn: Code 6063

Naval Surface Weapons
Center
White Oak, MD 20910
Attn: Code R30
Technical Library

Naval Surface Weapons
Center
Dahlgren, VA 22448
Attn: Technical Library

Naval Civil Eng Library
Port Hueneme, CA 93043
Attn: Technical Library

Naval Underwater Systems
Center
New London, CT 06320
Attn: Code 44
Technical Library

Naval Underwater Systems
Center
Newport, RI 02841
Attn: Technical Library

Naval Weapons Center
China Lake, CA 99555
Attn: Technical Library

NRL/Underwater Sound
Reference Dept.
Orlando, FL 32856
Attn: Technical Library

Chief of Naval Operations
Department of the Navy
Washington, DC 20350
Attn: Code OP-098

Commander
Naval Sea Systems Command
Washington, DC 20362
Attn: Code 05R25

Commander
Naval Sea Systems Command
Washington, DC 20362
Attn: Code 05R26

Commander
Naval Sea Systems Command
Washington, DC 20362
Attn: Code 09B31

Commander
Naval Sea Systems Command
Washington, DC 20362
Attn: Code 55Y

Commander
Naval Sea Systems Command
Washington, DC 20362
Attn: Code 55Y2

Commander
Naval Sea Systems Command
Washington, DC 20362
Attn: Code 03D

Commander
Naval Sea Systems Command
Washington, DC 20362
Attn: Code 7226

Commander
Naval Sea Systems Command
Washington, DC 20362
Attn: Code 310A

Commander
Naval Sea Systems Command
Washington, DC 20362
Attn: Code 3108

US Naval Academy
Mechanical Engineering Dept.
Annapolis, MD 21402

Naval Postgraduate School
Monterey, CA 93940
Attn: Technical Library

Mr. Jerome Persh
Stf Specit for Matls &Struct
OUSDE & E. The Pentagon
Room 301089
Washington, DC 20301

Professor J. Hutchinson
Harvard University
Div. of Applied Sciences
Cambridge, MA 02138

Dr. Harold Liebowitz, Dean
School of Engr. & Applied Sci.
George Washington
University
Washington, DC 20052

Professor G.T. Hahn
Vanderbilt University
Dept. of Mech. & Matls. Engr.
Nashville, TN 37235

Professor Albert S.
Kobayashi
Dept. of Mechanical
Engineering
University of Washington
Seattle, WA 98195

Professor L.B. Freund
Brown University
Division of Engineering
Providence, RI 02912

Professor B. Budiansky
Harvard University
Division of Applied Sciences
Cambridge, MA 02138

Professor S.N. Atluri
Georgia Institute of
Technology
School of Engr. & Mechanics
Atlanta, GA 30332

Professor G.Springer
Stanford University
Dept. of Aeronautics
& Astronautics
Stanford, CA 94305

Professor H.T. Hahn
Dept of Engr Sciences &
Mech
Penn State University
227 Hammond Bldg
University Park, PA 16802

Professor S.K. Datta
University of Colorado
Dept. of Mechanical
Engineering
Boulder, CO 80309

Dr. M.L. Williams
School of Engineering
University of Pittsburgh
Pittsburgh, PA 15261

Professor R.H. Gallagher
President
Clarkson University
Potsdam, NY 13676

Dr. D.C. Drucker
Dept. of Aerospace Eng.
& Mechanics
University of Florida
Tallahassee, FL 32611

Professor B.A. Boley
Dept. of Civil Engineering
Columbia University
New York, NY 10025

Professor J. Duffy
Brown University
Division of Engineering
Providence, RI 02912

Professor J.D. Achenbach
Northwestern University
Dept of Civil Engineering
Evanston, IL 60208

Professor F.A. McClintock
Dept of Mechanical
Engineering
Massachusetts Institute of
Technology
Cambridge, MA 02139

Professor D.M. Parks
Dept of Mechanical
Engineering
Massachusetts Institute of
Technology
Cambridge, MA 02139

Dr. M.F. Kanninen
Southwest Research
Institute
PO Drawer 28510
6220 Culebra Road
San Antonio, TX 78284

Professor F.P. Chiang
Dept of Mechanical Engr
State U of NY at Stony Brook
Stony Brook, NY 11794

Professor S.S. Wang
Dept of Theoretical & Appl
Mechs
University of Illinois
Urbana, IL 61801

Professor Y. Weitsman
Civil Engr Department
Texas A&M University
College Station, TX 77843

Professor I.M. Daniel
Dept of Mechanical Engr
Northwestern University
Evanston, IL 60208

Professor C.T. Sun
School of Aeronautics
& Astronautics
Purdue University
W. Lafayette, IN 47907

Professor J. Awerbuch
Dept of Mech Engr &
Mechanics
Drexel University
Philadelphia, PA 19104

Professor T.H. Lin
University of California
Civil Engineering Dept
Los Angeles, CA 90024

Professor G.J. Dvorak
Dept of Civil Engr
Rensselaer Polytecnic
Institute
Troy, NY 12180

Dr. R.M. Christensen
Chemistry & Mtrl Sci Dept
Lawrence Livermore Natl
Lab
PO Box 80P
Livermore, CA 94550

Professor J.R. Rice
Division of Applied Sciences
Harvard University
Cambridge, MA 02138

Professor W.N. Sharpe
The Johns Hopkins
University
Dept of Mechanics
Baltimore, MD 21218

Professor C.F. Shih
Brown University
Division of Engineering
Providence, RI 02912

Professor A. Rosakis
California Institute of Tech
Graduate Aeronautical Labs
Pasadena, CA 91125

Professor D. Post
VA Polytechnic & State U
Dept of Engr Science &
Mechanics
Blacksburg, VA 24061

Professor W. Sachse
Cornell University
Dept of Theoretical &
Applied Mechanics
Ithaca, NY 14853

UNCLASSIFIED

SECURITY CLASSIFICATION OF THIS PAGE *(When Data Entered)*

REPORT DOCUMENTATION PAGE		READ INSTRUCTIONS BEFORE COMPLETING FORM
1. REPORT NUMBER UWA/DME/TR-87/58	2. GOVT ACCESSION NO.	3. RECIPIENT'S CATALOG NUMBER
4. TITLE *(and Subtitle)* "Toughening of a Particulate-Reinforced/Ceramic-Matrix Composite"		5. TYPE OF REPORT & PERIOD COVERED Technical Report 6. PERFORMING ORG. REPORT NUMBER UWA/DME/TR-85/51
7. AUTHOR(s) M.S. Taya, S. Hayashi, A.S. Kobayashi, H.S. Yoon		8. CONTRACT OR GRANT NUMBER(s) N000-14-87-K-0326
9. PERFORMING ORGANIZATION NAME AND ADDRESS Department of Mechanical Engineering, FU-10 University of Washington Seattle, Washington 98195		10. PROGRAM ELEMENT, PROJECT, TASK AREA & WORK UNIT NUMBERS
11. CONTROLLING OFFICE NAME AND ADDRESS Office of Naval Research Arlington, VA 22217-5000		12. REPORT DATE September 1989 13. NUMBER OF PAGES 35
14. MONITORING AGENCY NAME & ADDRESS*(if different from Controlling Office)*		15. SECURITY CLASS. *(of this report)* UNCLASSIFIED 15a. DECLASSIFICATION/DOWNGRADING SCHEDULE

16. DISTRIBUTION STATEMENT *(of this Report)*

Unlimited

17. DISTRIBUTION STATEMENT *(of the abstract entered in Block 20, if different from Report)*

18. SUPPLEMENTARY NOTES

19. KEY WORDS *(Continue on reverse side if necessary and identify by block number)*

Toughening mechanism, particulate-reinforced/ceramic-matrix composite, thermal residual stress, crack deflection model, Eshelby's model, coefficient of thermal expansion.

20. ABSTRACT *(Continue on reverse side if necessary and identify by block number)*

The toughening mechanism of particulate-reinforced/ceramic-matrix composite was attributed to the thermal residual stress field induced by the differential thermal expansions of the matrix and the particulate when the composite is cooled from the processing to room temperature. The measured increase of 77 percent in toughness in a TiB_2-particulate/SiC-matrix ceramic composite compared well with the predicted increase of 52 percent.

DD FORM 1 JAN 73 1473 EDITION OF 1 NOV 65 IS OBSOLETE
S/N 0102-014-6601

UNCLASSIFIED

SECURITY CLASSIFICATION OF THIS PAGE *(When Data Entered)*